Radio emission from colliding outflows in high-mass X-ray binaries with strongly magnetized neutron stars

Margaritis Chatzis, Maria Petropoulou, Georgios Vasilopoulos

Monthly Notices of the ROYAL ASTRONOMICAL SOCIETY

MNRAS **509,** 2532–2550 (2022) https://doi.org/10.1093/mnras/stab3098
Advance Access publication 2021 October 26

Radio emission from colliding outflows in high-mass X-ray binaries with strongly magnetized neutron stars

Margaritis Chatzis,[1]★ Maria Petropoulou [2]★ and Georgios Vasilopoulos [3,4]★

[1]*Department of Physics, University of Crete, GR-71003 Heraklion, Greece*
[2]*Department of Physics, National and Kapodistrian University of Athens, University Campus Zografos, GR-15783 Athens, Greece*
[3]*Université de Strasbourg, CNRS, Observatoire Astronomique de Strasbourg, F-67000 Strasbourg, France*
[4]*Department of Astronomy, Yale University, PO Box 208101, New Haven, CT 06520-8101, USA*

Accepted 2021 October 22. Received 2021 October 22; in original form 2021 September 21

ABSTRACT

We present a toy model for radio emission in high-mass X-ray binaries (HMXBs) with strongly magnetized neutron stars (NSs) where a wind-collision region is formed by the NS outflow and the stellar wind of the massive companion. Radio emission is expected from the synchrotron radiation of shock-accelerated electrons and the free–free emission of the stellar wind. We found that the predicted relation between the GHz luminosity ($L_{\rm R}$) and the accretion X-ray luminosity ($L_{\rm X}$) can be written as $L_{\rm R} \propto L_{\rm X}^{b}$ for most parameters. No correlation with X-rays is expected ($b = 0$) when the thermal emission of the stellar wind dominates in radio. We typically find a steep correlation ($b = 12/7$) for sub-Eddington X-ray luminosities and a more shallow one [$b = 2(p - 1)/7$] for super-Eddington X-ray luminosities, where p is the power-law index of accelerated electrons. The maximum predicted radio luminosity is independent of the NS properties, while it depends on the stellar wind momentum, binary separation distance, and the minimum electron Lorentz factor. Using a Bayesian approach, we modelled the radio observations of Swift J0243.6+6124 that cover a wide range of mass accretion rates. Our results support a shock origin for the radio detections at sub-Eddington X-ray luminosities. However, no physically meaningful parameters could be found for the super-Eddington phase of the outburst, suggesting a different origin. Future observations with more sensitive instruments might reveal a large number of HMXBs with strongly magnetized NSs in radio, allowing the determination of the slope in the $L_{\rm R}$–$L_{\rm X}$ relation, and putting the wind-collision scenario into test.

Key words: stars: neutron – X-rays: binaries – radiation mechanism: non-thermal, thermal.

1 INTRODUCTION

X-ray binaries (XRBs) are systems where mass is transferred from a donor star on to a compact object while its dynamical energy is converted to radiation. XRBs that host stellar mass black holes or neutron stars (NSs) with low magnetic fields (i.e. $<10^9$ G) tend to spent most of their lives in quiescence but occasionally undergo major outbursts that may reach or exceed the Eddington limit. Studies of the outburst/quiescence cycle of such systems have revealed dramatic changes in their X-ray spectral characteristics and temporal properties along with changes in their luminosity (McClintock & Remillard 2006). The main spectral states during outbursts are known as the hard state, which is characterized by a Comptonized X-ray spectrum, and the soft state, which is dominated by thermal emission from an accretion disc. Moreover, multiwavelength observations have revealed the presence of radio emission associated with a compact jet during the hard and quiescent state, providing evidence for a correlation between the radio and X-ray fluxes (e.g. Hannikainen et al. 1998; Gallo, Fender & Pooley 2003; Markoff et al. 2003; Corbel et al. 2004, 2013a).

In fact, the radio/X-ray correlation is a key piece of observational evidence about the disc–jet (or inflow–outflow) connection in XRBs. The 'universal' radio/X-ray flux correlation ($L_{\rm R} \propto L_{\rm X}^{0.6}$) seems to hold for most BH XRBs in low-hard flux states, although data are dominated by two systems, GX 339−4 and V404 Cyg (e.g. Gallo, Miller & Fender 2012; Corbel et al. 2013a), and more recently MAXI J1820+070 (Bright et al. 2020). This relation holds even for some of the faintest BH systems like A0620−00 (Gallo et al. 2006; Dinçer et al. 2018) and XTE J1118+480 (Gallo et al. 2014). However, the radio/X-ray luminosity plane contains outliers like H 1743−322 (Coriat et al. 2011), where the correlation is steeper ($L_{\rm R} \propto L_{\rm X}^{1.4}$) and quite similar to the one found in the few reported NS XRBs (e.g. Migliari & Fender 2006).

Till recently, radio emission associated with jets was thought to be a unique property of BH XRBs or those hosting weakly magnetized NSs (i.e. $<10^9$ G). However, the narrative changed following deep observations with the Very Large Array (VLA) telescope that led to the discovery of radio emission from the prototypical X-ray pulsar Her X−1 (van den Eijnden et al. 2018a) and the symbiotic XRB GX 1+4 (van den Eijnden et al. 2018b). More recently, X-ray pulsars Swift J0243.6+6124 and 1A 0535+262 were detected in radio during major outbursts (van den Eijnden et al. 2018c, 2020). Both of these systems are high-mass X-ray binaries (HMXBs) with a Be donor (i.e. BeXRBs; Reig 2011). BeXRBs are quite different

★ E-mail: mpetropo@phys.uoa.gr (MP); ph5123@edu.physics.uoc.gr (MC); georgios.vasilopoulos@astro.unistra.fr (GV)

than BH XRBs, for in BeXRBs material escapes the massive donor through a slow-moving equatorial outflow, which is usually referred as decretion disc or Be disc (e.g. Krtička, Owocki & Meynet 2011). The disc itself is quite complex and can be described as a circumstellar environment with atomic, molecular, and dusty regions usually found in rings or disc-like structures (e.g. Maravelias et al. 2018). BeXRBs are quite variable showing two types of outbursts. Type I outbursts ($L_X \sim 10^{36}$ erg s^{-1}) may occur during a close passage of the NS to the decretion disc and thus show a correlation with the binary orbital period. Giant or Type II outbursts ($L_X \geq 10^{38}$ erg s^{-1}) that can last for several orbits might be associated with wrapped Be discs (Okazaki, Hayasaki & Moritani 2013). During outbursts, an accretion disc is formed around the NS, which may be truncated at very large radii (100–1000 km) due to the large magnetic field of the NS (typically $>10^{12}$ G). Matter is then accreted following the magnetic field lines on to the NS surface forming a thermal mount of material, the so-called accretion column (Basko & Sunyaev 1976). The accretion column is responsible for the bulk of the X-ray emission and any disc contribution is usually negligible at sub-Eddington luminosities.[1]

The physical interpretation of the radio/X-ray correlation in BH XRBs has been widely discussed in the literature. While it is well established that during the low-hard states radio is produced by synchrotron-emitting electrons in a compact jet, the origin of the X-ray emission is less clear; X-rays could be a part of the optically thin jet-synchrotron spectrum (e.g. Markoff, Falcke & Fender 2001; Markoff et al. 2003; Merloni, Heinz & di Matteo 2003; Falcke, Körding & Markoff 2004) or they could arise from a radiatively inefficient accretion flow or a radiatively efficient disc–corona system (e.g. Heinz & Sunyaev 2003; Merloni et al. 2003; Maccarone 2005; Yuan, Cui & Narayan 2005). In the case of highly magnetized X-ray pulsars, understanding the coupling of radio and X-ray emissions can be even more complicated. On the one hand, no jet structure has been resolved in any of the radio-detected accreting X-ray pulsars, so even the origin of the radio emission is less certain. On the other hand, the detected X-ray emission is mainly produced in the accretion column, close to the NS surface. Hence, even if the radio emission had a jet origin in X-ray pulsars, X-rays would still be produced in another region with different physical conditions, such as plasma densities and magnetic fields. In the latter case, deriving a relation coupling the X-ray and radio luminosities would require theoretical understanding of the jet formation in highly magnetized accreting pulsars, which is far from being settled. Further observational studies of the L_R and L_X evolution during outbursts as well as in low-flux states should be tested against theoretical predictions to better understand the physical connection behind this phenomenon.

1.1 The case of Swift J0243.6+6124

For Her X−1, it was originally proposed that the radio could be due to a synchrotron-emitting radio jet (van den Eijnden et al. 2018a). Swift J0243.6+6124 (hereafter J0243) was the first Galactic source that exceeded by a factor of 10 the Eddington limit for a NS (Wilson-Hodge et al. 2018), and was thus classified as a transient ultra-luminous X-ray pulsar (ULXPs; see review by Kaaret, Feng & Roberts 2017). Its high luminosity and proximity made the source an ideal target for multiwavelength monitoring, resulting in the first detection of radio emission from a BeXRB during an outburst. The radio jet scenario from an X-ray pulsar was reinforced following the initial discovery of correlated radio and X-ray emission from J0243 during the super-Eddington phase of the 2017–2018 outburst (van den Eijnden et al. 2018c). However, extended monitoring of J0243 during the low-flux state revealed a quite puzzling behaviour between radio and X-ray emission (van den Eijnden et al. 2019a), with bright radio states as the source returned to a low X-ray flux state showing moderate type-I X-ray outbursts.

A solution proposed to explain these radio detections is based on the notion that a jet quickly re-establishes by driving the magnetospheric radius inwards and outwards with respect to the co-rotation radius when a certain X-ray luminosity level is crossed. However, such a hypothesis has certain caveats. The time-scale for the reappearance of the jet is remarkably shorter than that in other XRBs, taking only some days instead of the usual one to a few weeks (e.g. Corbel et al. 2013b; van der Horst et al. 2013). Moreover, the launching site of the jet is not well understood (e.g. Massi & Kaufman Bernadó 2008; Parfrey, Spitkovsky & Beloborodov 2016) while all further calculations require an a priori assumption that the launch originates within the truncated disc (e.g. van den Eijnden et al. 2018c).

Another possibility to explain the radio emission is to consider that accreting HMXBs can launch outflows. These outflows can be launched during phases characterized by high accretion as those encountered in HMXB outbursts or in persistent ULXs (see e.g. Shakura & Sunyaev 1973; Middleton et al. 2021, for some theoretical predictions). State-of-the-art numerical simulations also show the formation of outflows in super-Eddington ULXPs (e.g. Takahashi & Ohsuga 2017; Abarca, Parfrey & Kluźniak 2021) and in low-luminosity accreting systems (e.g. Parfrey & Tchekhovskoy 2017). Moreover, absorption features consistent with fast relativistic outflows have been observed in spectral studies of ULXPs (e.g. Kosec et al. 2018; van den Eijnden et al. 2019b) or have been indirectly probed in order to explain their overall temporal properties (e.g. Mushtukov et al. 2019; Vasilopoulos et al. 2019, 2020). These outflows can collide with wind from the donor star creating a shock-accelerated population of relativistic electrons that emits in radio frequencies. This thought, that colliding winds can produce a substantial amount of radio emission, is not unfounded. The radio emission of a plethora of massive binaries (e.g. Wolf–Rayet OB stars) can be explained by synchrotron emission originating in the wind-collision region (e.g. Abbott et al. 1986; Eichler & Usov 1993; Dougherty et al. 2003; Pittard et al. 2006; De Becker & Raucq 2013). The possibility that the radio emission comes from shocks between the accretion disc wind and the wind of a Wolf–Rayet donor star has also been discussed in the context of the microquasar Cygnus X−3 in its hypersoft X-ray state (Koljonen et al. 2018).

Motivated by the above, we will explore a scenario where radio emission is produced in the collision region of the NS outflow and the Be wind. We will build a toy model for computing synchrotron emission from shock-accelerated electrons taking into account synchrotron self-absorption, free–free absorption by the stellar wind, and Razin suppression due to background plasma. The contribution of the Be wind in radio frequencies due to free–free emission will also be considered. Our goal is to check whether substantial radio emission can be produced from the system of colliding outflow wind, and if so, what is the predicted relation between radio and X-ray luminosities. As a test case for our model, we will use J0243, for it is the only system with multiple radio detections that map a wide range of mass accretion rates.

[1]The Eddington luminosity is defined as $L_{Edd} \simeq 1.5 \times 10^{38}\, M_{NS}/M_\odot$ erg s^{-1}.

Table 1. Stellar wind models.

Model	$\dot{M}_{\rm Be}$ ($10^{-9}\,{\rm M}_\odot\,{\rm yr}^{-1}$)	$V_{\rm Be}^{\infty}$ (km s^{-1})
W1	1	3000
W2	10	3000
W3	100	3000
W4	1	1500
W5	1	500

Note. A common wind temperature of 2.5×10^4 K is assumed.

This paper is structured as follows. In Section 2, we outline the model used to compute the radio emission and present our results in Section 3. In Section 4, we apply our model to the multi-epoch radio observations of J0243. We continue with a discussion of our results and model caveats in Section 5. We conclude with a summary of our main findings in Section 6.

2 MODEL DESCRIPTION

In this section, we will describe our toy model for the calculation of radio emission from HMXBs with highly magnetized NSs, while highlighting the main assumptions entering our calculations. We will first describe the assumed geometry of the system (Section 2.1) and then the radiative processes considered (Section 2.2).

2.1 A system of colliding outflows

We consider a binary system composed of a NS and a Be star. The companion, being a massive early-type star, loses mass at much higher rates than a solar-like star. Be stars are known to lose mass predominantly through equatorial winds, but they also possess an extended wind region composed of low-density fast-moving plasma (for a review, see Porter & Rivinius 2003). Evidence for such anisotropic winds has been recently reported in interacting wind systems through X-ray observations (e.g. Petropoulou et al. 2018; Chernyakova et al. 2020). In our toy model, we assume, however, a spherically symmetric (non-clumpy) wind with constant mass-loss rate $\dot{M}_{\rm Be}$. We do not consider the acceleration of the Be wind in our calculations. Instead, we assume that the wind is coasting with its terminal velocity, $V_{\rm Be}^{\infty}$. The mass-loss rate of early-type stars in the main sequence strongly depends on the stellar effective temperature. For instance, the hottest B stars ($T_{\rm eff} \simeq 3 \times 10^4$ K) with masses $M \sim 12\,{\rm M}_\odot$ have $\dot{M}_{\rm Be} \sim 10^{-9}\,{\rm M}_\odot\ {\rm yr}^{-1}$, while the cooler and less massive ones (e.g. $T_{\rm eff} \lesssim 2 \times 10^4$ K and $M \lesssim 7\,{\rm M}_\odot$) exhibit weaker winds with mass-loss rates lower even by three orders of magnitude (Krtička 2014). Mass-loss rates as high as $\sim 10^{-7}\,{\rm M}_\odot\ {\rm yr}^{-1}$ have also been theoretically predicted for the more luminous and massive B stars (Vink, de Koter & Lamers 2000). Typical values for the terminal wind velocity are $V_{\rm Be}^{\infty} \simeq 500$–$5000$ km s^{-1} (e.g. Kudritzki & Puls 2000; Vink et al. 2000; Krtička 2014). When the irradiation from the X-ray-emitting NS on to the stellar wind is taken into account, slowing down or even suppression of the wind is predicted (Krtička, Kubát & Krtičková 2015). Such feedback effects are, however, not included in our toy model. To account for the range of values in stellar wind properties (found theoretically and observationally), we consider five wind models with different mass-loss rates and terminal velocities that are summarized in Table 1. For simplicity, we also adopt a common wind temperature of 2.5×10^4 K, as this does not affect our main results.

Strong disc winds/outflows have been commonly observed during outbursts in low-mass XRBs (e.g. Oosterbroek et al. 1997; Tetarenko et al. 2018). However, persistent mass-loss from the disc has been predicted across different spectral states by radiation-hydrodynamic simulations (Higginbottom et al. 2020). In the case of magnetized NSs, disc outflows are also expected at sufficiently high mass accretion rates (Shakura & Sunyaev 1973; King & Lasota 2016) and have been observed in ULXPs (e.g. Koliopanos & Vasilopoulos 2018; van den Eijnden et al. 2019b; Kosec et al. 2021). From a theoretical standpoint, if the accretion is locally super-Eddington, namely the mass accretion rate exceeds the critical rate[2] $\dot{M}_{\rm Edd} \simeq 2.3 \times 10^{17}\, M_{\rm NS}/(1.4\,{\rm M}_\odot)$ g s^{-1}, part of the dissipated energy in the disc is used to launch outflows from within the so-called spherization radius (Shakura & Sunyaev 1973). Recently, state-of-the-art simulations have revealed that these outflows can be strong enough to result in optically thick funnel-like structures (Abarca et al. 2021). In addition, apart from the super-Eddington regime, outflows can be formed in low accretion rates from the inner disc radius following its interaction with the NS magnetic field lines (Parfrey & Tchekhovskoy 2017). Thus, it is clear that outflows can occur in a large variety of systems and conditions for BH and magnetized NS accretors.

In contrast to non-magnetized accreting objects, the accretion discs around magnetized NSs do not extend to the innermost stable orbit, but they are truncated at much larger radii due to the interaction with the NS magnetic field. The magnetospheric radius provides an estimate of the disc inner radius (Ghosh, Lamb & Pethick 1977):

$$R_{\rm M} = \xi \left(\frac{R_{\rm NS}^{12} B_{\rm NS}^{4}}{2 G M_{\rm NS} \dot{M}^2} \right)^{1/7}, \tag{1}$$

where G is the gravitational constant, $R_{\rm NS}$ is the NS radius, $B_{\rm NS}$ is the polar magnetic field strength of the NS, $\dot{M}$ is the accretion rate on to the NS, and $\xi \sim 0.5$ is a model-dependent parameter related to the coupling of the NS magnetic field with the disc (Campana et al. 2018). For typical magnetic field strengths in X-ray pulsars (e.g. 10^{12} G), very high mass accretion rates are required (e.g. $> 10\,\dot{M}_{\rm Edd}$ or $L_{\rm X} \gtrsim 10^{39}$ erg s^{-1}) to push the NS magnetosphere within the spherization radius.

In our toy model, we do not specify the origin of the NS outflow and postulate that it is present regardless of the accretion regime. The outflow is also assumed to be spherically symmetric and homogeneous (i.e. non-clumpy). The rate at which mass is carried away from the NS is parametrized as $\dot{M}_{\rm NS} = \eta_{\rm out} L_{\rm X}/(\epsilon c^2)$, where c is the speed of light, $\epsilon \sim 0.2$ is the accretion efficiency on to the NS (e.g. Vasilopoulos et al. 2019), and $\eta_{\rm out} < 1$ is the fraction of the accreted mass lost through the outflow. The NS outflow speed is considered constant and proportional to the Keplerian velocity at $R_{\rm M}$, which is a proxy of the inner disc radius, namely $V_{\rm NS}^{\infty} = \chi \sqrt{G M_{\rm NS}/R_{\rm M}}$. Here, $\chi \sim 1$–3 to allow for an accelerating outflow.

If the binary separation distance is large enough, the two stellar winds can collide at high speeds, forming the so-called wind colliding region (WCR; Usov 1992). Neglecting the effects of the orbital motion and under the assumption of spherically symmetric and homogeneous outflows, the WCR is almost spherical at small angles as measured from the line connecting the centres of the two stars, and becomes conical only at large angles (Usov 1992; Eichler & Usov 1993). The apex of the shock on the axis that connects the two stars is located at a distance $d_{\rm NS}$ and $d_{\rm Be}$ from the NS and Be star, respectively (see also Fig. 1). Assuming spherical colliding winds,

[2]This is defined as $\dot{M}_{\rm Edd} = L_{\rm Edd}/c^2$.

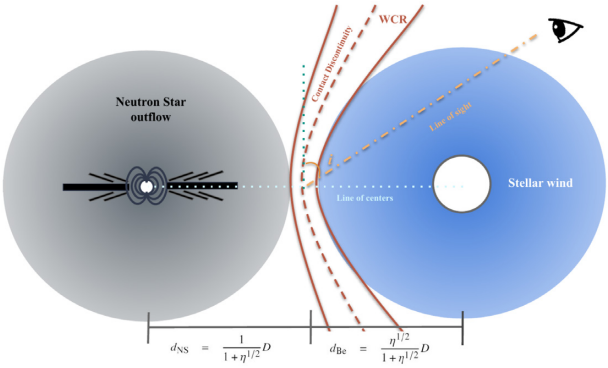

Figure 1. A schematic illustration of our toy model (not in scale).

these distances are written as (Eichler & Usov 1993)

$$d_{\rm NS} = \frac{1}{1+\eta^{1/2}} D \tag{2}$$

$$d_{\rm Be} = \frac{\eta^{1/2}}{1+\eta^{1/2}} D, \tag{3}$$

where D is the binary separation distance and η is the wind momentum ratio that is defined as

$$\eta = \frac{\dot{M}_{\rm Be} V_{\rm Be}^{\infty}}{\dot{M}_{\rm NS} V_{\rm NS}^{\infty}}. \tag{4}$$

If $\eta > 1$ (i.e. the Be wind is stronger than the NS outflow), the shock will be wrapped around the NS and $d_{\rm NS} < d_{\rm Be}$. However, for typical Be stellar wind parameters and super-Eddington accretion rates, the opposite situation may be realized, as illustrated in Fig. 1. In both cases, the shock radius, $R_{\rm sh}$, is measured from the centre of the star that is closer to the shock, i.e. $R_{\rm sh} = \min(d_{\rm NS}, d_{\rm Be})$. Parameter values leading to $R_{\rm sh} < R_{\rm NS}$ or $R_{\rm sh} \lesssim 20\,{\rm R}_{\odot}$ are ignored as being non-physical. The latter is a loose limit for the radial distance in which the wind acceleration is completed (e.g. Friend & Abbott 1986; Lamers & Cassinelli 1999).

2.2 Radio emission from the system

Astrophysical shocks can accelerate charged particles to high energies as indicated by the associated non-thermal emission. First-order Fermi acceleration, according to which particles gain energy through repeated shock crossings mediated by scattering off magnetic perturbations on both sides, is thought to be the main acceleration mechanism at play (Bell 1978; Blandford & Ostriker 1978; Drury 1983). The energy distribution of accelerated particles is found to be a power law, i.e. $N(E) \propto E^{-p}$, with the index p depending on the shock compression ratio r. For strong shocks, $r = 4$ and $p \simeq 2$.

Strong shocks formed by the colliding stellar winds in massive binary systems have been discussed as promising sites of particle acceleration and non-thermal radiation (e.g. Eichler & Usov 1993; Dougherty et al. 2003; Pittard, Romero & Vila 2021). In our toy model, we assume that relativistic electrons are produced by first-order Fermi acceleration at the shocks of the colliding stellar wind and NS outflow, and compute the synchrotron emission produced in the region of the shocked stellar wind.[3]

A vital quantity for this calculation is the energy density of the shocked wind region $U_{\rm Be}$. In order to calculate said quantity, we employ our knowledge that for a strong shock we have $U_{\rm Be} = (9/8)\rho(V_{\rm Be}^{\infty})^2$, where $\rho = \dot{M}_{\rm Be}/4\pi d_{\rm Be}^2 V_{\rm Be}^{\infty}$ is the pre-shock wind density at distance $d_{\rm Be}$. Thus, in terms of η and our wind parameters we have

$$U_{\rm Be} = \frac{9}{32\pi} \dot{M}_{\rm Be} V_{\rm Be}^{\infty} D^{-2} \left(1+\eta^{-1/2}\right)^2. \tag{5}$$

Accordingly, we can calculate the total electron energy density of the shocked electron population by attributing to it a fraction of the total energy density, namely $U_{\rm e} = \epsilon_{\rm e} U_{\rm Be}$, while assigning the rest to the energy density of the post-shock magnetic field, that is $U_{\rm B} = \epsilon_{\rm B} U_{\rm Be}$.

The energy distribution of the accelerated electrons per unit volume is modelled as a power law extending from a minimum to a maximum Lorentz factor ($\gamma_{\rm min}$ and $\gamma_{\rm max}$, respectively) with a slope of p, namely $n(\gamma) \equiv {\rm d}N/{\rm d}\gamma{\rm d}V = K_{\rm e}\gamma^{-p}$, $\gamma_{\rm min} \leq \gamma \leq \gamma_{\rm max}$. Here, $K_{\rm e}$ is the normalization factor that is directly related to the total electron energy density via $U_{\rm e} = m_{\rm e}c^2 \int_{\gamma_{\rm min}}^{\gamma_{\rm max}} n(\gamma)(\gamma-1){\rm d}\gamma$. Even though index p is related to the shock compression ratio, our model is not designed to describe the acceleration process. Hence, we consider $p \geq 2$ a free parameter of the model. For the same reasons, we also let $\gamma_{\rm min}$ to be a free parameter and assume that $\gamma_{\rm max} \gg \gamma_{\rm min}$.

Relativistic electrons in the WCR can cool (i.e. lose energy) due to synchrotron radiation and inverse Compton (IC) scattering on stellar photons. As a result of synchrotron and/or IC cooling (in the Thomson regime), the power-law slope of the accelerated electron population steepens by one, i.e. $N(\gamma) \sim \gamma^{-p-1}$, for values of γ above a critical Lorentz factor, known as the cooling Lorentz factor. This is estimated by balancing the radiative loss time-scale, $t_{\rm loss}$, with a typical time-scale, $t_{\rm dyn}$, on which particles are advected along the contact discontinuity. The cooling time-scale for an electron with Lorentz factor γ due to synchrotron and IC losses in the Thomson regime[4] is $t_{\rm loss} \approx 3\pi m_{\rm e} c/[4\sigma_{\rm T}(U_{\rm B}+U_{\rm ph})\gamma]$. Here, $U_{\rm ph} \approx L_{\rm Be}/4\pi c\, d_{\rm Be}^2$ is a proxy for the energy density of stellar photons that are up-scattered by the electrons in the WCR (e.g. Pittard et al. 2006). We adopt $L_{\rm Be} = 10^4\,{\rm L}_{\odot}$ as a typical value for the bolometric luminosity of the Be star. For simplicity, we set $t_{\rm dyn} \approx R_{\rm sh}/(rV)$, where $V \approx V_{\rm Be}^{\infty}/r$ is the post-shock flow velocity and $r \approx 4$ is the shock compression ratio. In reality, the advection velocity will depend on the position along the contact discontinuity (e.g. Johnstone et al. 2015), but this cannot be captured by the single zone nature of our toy model. The cooling Lorentz factor due to synchrotron and IC losses in the Thomson limit is then written as

$$\gamma_{\rm c} = \frac{3 m_{\rm e} c V_{\rm Be}^{\infty}}{4\sigma_{\rm T}(U_{\rm B}+U_{\rm ph}) R_{\rm sh}}, \tag{6}$$

where $m_{\rm e}$ is the electron mass. For most parameter combinations we consider, we find that $\gamma_{\rm c} > \gamma_{\rm min}$ (slow-cooling regime; Sari, Piran & Narayan 1998) with lower $\gamma_{\rm c}$ values obtained whenever the WCR is pushed very close to the Be star (i.e. for strong NS outflows and/or weak Be winds). In the latter case, IC cooling dominates the energy losses and can even lead to $\gamma_{\rm c} \ll \gamma_{\rm min}$ (fast-cooling regime; Sari et al. 1998). Fast-cooling electrons would be confined to regions close to the shocks and would not occupy the full width of the WCR, resulting in a smaller emitting volume than the one for slow-cooling electrons (e.g. Pittard et al. 2006). This effect is not captured by our toy model. Moreover, the point-source approximation for the calculation of $U_{\rm ph}$ would break down when the WCR would form

[3]For the calculation of non-thermal emission, we consider only the spherical part of the WCR.

[4]Electrons with Lorentz factors up to $\sim m_{\rm e}c^2/\epsilon \simeq 5 \times 10^5 (1\,{\rm eV}/\epsilon)$ can up-scatter stellar photons of energy ϵ in the Thomson regime.

Table 2. Default values of model parameters.

Parameter	Symbol	Value
NS magnetic field strength	$B_{\rm NS}$	10^{12} G
NS radius	$R_{\rm NS}$	10^{6} cm
NS mass	$M_{\rm NS}$	$1.4\,{\rm M}_{\odot}$
Be bolometric luminosity	$L_{\rm Be}$	$10^{4}\,{\rm L}_{\odot}$
Ratio of NS outflow velocity and Keplerian velocity at inner radius	χ	2
Fraction of accreted mass lost through outflows	$\eta_{\rm out}$	0.01
Radiative efficiency of accretion flow	ϵ	0.2
Fraction of magnetic field energy density	$\epsilon_{\rm B}$	0.5
Fraction of relativistic electron energy density	$\epsilon_{\rm e}$	0.5
Power-law index of electron energy distribution	p	2
Minimum electron Lorentz factor	$\gamma_{\rm min}$	10
Binary separation distance	D	$10^{3}\,{\rm R}_{\odot}$
Inclination angle	i	$\pi/4$

close to the Be star. Notably, most of the fast cooling cases are realized for $d_{\rm Be} < 20\,{\rm R}_{\odot}$ (non-physical solutions). For these reasons, we focus on the slow-cooling regime from this point on.

Having specified the above, we are able to derive the synchrotron emission accounting for possible suppression stemming from attenuation processes, such as synchrotron self-absorption within the shocked wind region and free–free absorption from the unshocked stellar wind. Moreover, in the presence of a background plasma, the synchrotron emission of a relativistic particle with Lorentz factor γ will be suppressed at low enough frequencies, since the beaming of the radiation is not as strong at frequencies $\gamma\omega_{\rm p}$, where $\omega_{\rm p}$ is the plasma frequency; this is known as the Razin effect (Razin 1960).

We can then write the intensity of the synchrotron radiation at frequency ν as

$$I_{\nu}^{\rm syn} = S_{\nu}^{\rm syn}\left(1-{\rm e}^{-\tau_{\nu}^{\rm ssa}}\right){\rm e}^{-\tau_{\nu}^{\rm ff}}{\rm e}^{-\nu_{\rm R}/\nu} \tag{7}$$

where $I_{\nu}^{\rm syn}$ is in units of erg cm^{-2} s^{-1} sr^{-1} Hz^{-1}. Here, we have the source function $S_{\nu}^{\rm syn} = j_{\nu}^{\rm syn}/a_{\nu}^{\rm ssa}$, with $j_{\nu}^{\rm syn}$ being the synchrotron emissivity, $a_{\nu}^{\rm ssa}$ the synchrotron self-absorption coefficient, $\tau_{\nu}^{\rm ssa} = a_{\nu}^{\rm ssa}R_{\rm sh}/4$ the optical depth for synchrotron self-absorption, $\tau_{\nu}^{\rm ff}$ the optical depth for free–free absorption, and $\nu_{\rm R} \simeq 20 n_{\rm sh}/B$ a critical frequency below which the Razin effect becomes important (e.g. Dougherty et al. 2003; Petropoulou, Kamble & Sironi 2016). Here, $n_{\rm sh} = 4\rho/(\mu m_{\rm p})$ represents the post-shock electron number density and μ is the mean molecular weight (0.6 for solar composition). The free–free optical depth along a path starting from the apex of the shock (see Fig. 1) can be written as (Wright & Barlow 1975)

$$\tau_{\nu}^{\rm ff} = K(\nu,T)A^2\,(d_{\rm Be}\cos{\rm i})^{-3}\int_{-i}^{\pi/2}\cos^2\theta\,{\rm d}\theta, \tag{8}$$

with

$$A = \frac{\dot{M}_{\rm Be}}{4\pi\mu{\rm m_H}{\rm V}_{\rm Be}^{\infty}} \tag{9}$$

and

$$K(\nu,T) = 3.7\times10^{8}\left(1-{\rm e}^{-{\rm h}\nu/{\rm kT}}\right)Z^2 g(\nu,T)T^{-1/2}\nu^{-3} \tag{10}$$

in cgs units. In the above expressions, i is the inclination angle (see also Fig. 1), $m_{\rm H}$ is the mass of the hydrogen atom, Z is the ion charge, $g(\nu, T)$ is the Gaunt factor, and T is the temperature of the Be wind. A more general expression of $\tau_{\nu}^{\rm ff}$ can be found in Appendix A.

Knowing the above, we can calculate the luminosity per unit frequency as

$$L_{\nu}^{\rm syn} = 4\pi{\rm R}_{\rm sh}^2{\rm I}_{\nu}^{\rm syn}{\rm f_V}, \tag{11}$$

where $f_{\rm V}$ is a fraction of a whole sphere. In our case, we take this to be $f_{\rm V} = 0.25$, corresponding to a spherical wedge from $-\pi/4$ to $+\pi/4$ above and below the line of centres (see Fig. 1). For larger angles, the approximation for a head-on collision of the winds at each point begins to break down (e.g. Pittard et al. 2021). Moreover, we calculate the thermal bremsstrahlung of the Be wind as (Wright & Barlow 1975)

$$L_{\nu}^{\rm th} = 141.9\,\zeta^{2/3}A^{4/3}B(\nu,T)K^{2/3}(\nu,T), \tag{12}$$

where the electron number density is assumed to be equal to ζ times the ion number density and $B(\nu, T)$ is the Planck function. Finally, the total observed luminosity per unit frequency is given by

$$L_{\nu}^{\rm obs} = L_{\nu}^{\rm th} + L_{\nu}^{\rm syn}. \tag{13}$$

3 RESULTS

Having described the set-up of our toy model, we move next in the calculation of the radio emission of the system for the wind models listed in Table 1. The parameter values used in all figures, if not otherwise noted, are summarized in Table 2.

3.1 Spectra

Spectra of the total emission computed using equation (13) are displayed for two values of the minimum electron Lorentz factor, i.e. $\gamma_{\rm min} = 10$ and 100 on the left- and right-hand panels of Fig. 2, respectively. The parameters describing the stellar wind are those of model W3, while $L_{\rm X} = 10^{38}$ erg s^{-1} is adopted. For these parameter values, the shock is wrapped around the Be star, as shown in Fig. 1. The total spectrum is composed of two components, namely the non-thermal synchrotron emission (dotted line) and the free–free emission of the Be stellar wind (dashed line). The synchrotron spectrum without accounting for free–free absorption is also shown for comparison (solid line). The spectral curvature seen below $\nu_{\rm ssa} \sim 1$ GHz is due to the Razin suppression. For most parameters considered in this work, free–free absorption is more important than the Razin suppression. The ordering of the synchrotron self-absorption frequency and the minimum characteristic synchrotron frequency ($\propto B\gamma_{\rm min}^2$) changes for the two values of $\gamma_{\rm min}$ considered here. This is illustrated by the change in slope of the synchrotron self-absorbed part of the spectrum. For the adopted parameter values, the non-thermal emission from the shocked wind starts to dominate the thermal wind emission at $\nu \sim 1$ GHz. The transition frequency from the thermal to the non-thermal component strongly

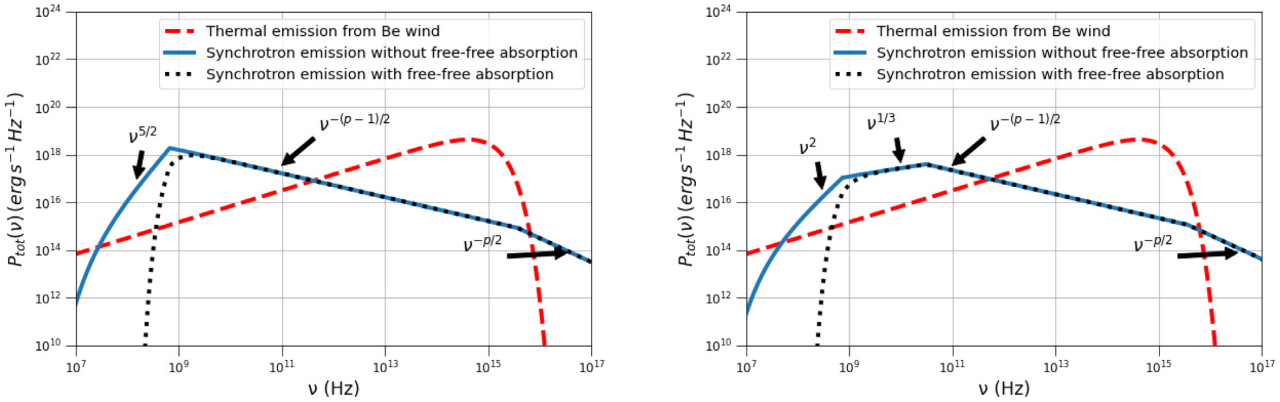

Figure 2. Spectral decomposition of the thermal and non-thermal emission of the system for $\gamma_{\rm min} = 10$ (left-hand panel) and $\gamma_{\rm min} = 100$ (right-hand panel). In both cases, the effect of the free–free absorption on the synchrotron emission is noted. Here, the stellar wind model W3 was used and $L_{\rm X} = 10^{38}$ erg s^{-1} was assumed. All other parameters used are listed in Table 2.

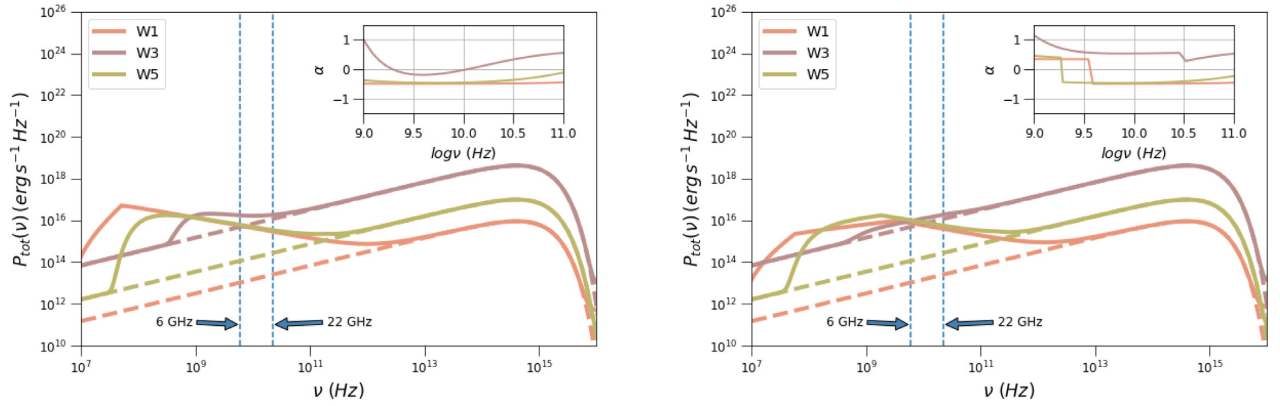

Figure 3. Radio-to-UV spectrum for three wind models and $L_{\rm X} = 10^{37}$ erg s^{-1}. Left- and right-hand panels show results for $\gamma_{\rm min} = 10$ and 100, respectively. Thick solid and dashed lines show the total emission and thermal wind emission, respectively. Vertical dashed lines indicate two characteristic radio frequencies. In a strong wind scenario, like W3, the 6 GHz emission is dominated by the Be stellar wind. Inset plots show $\alpha \equiv {\rm dlog}\, P_{\rm tot}(\nu)/{\rm dlog}\,\nu$ as a function of frequency between 1 and 100 GHz.

depends on the parameters, as we will illustrate later in this section. At lower frequencies, the free–free opacity becomes much larger than unity, thus significantly reducing the synchrotron flux. The thermal emission from the ionized stellar wind dominates again the overall emission between the infrared and UV wavelengths, with a peak at $\sim 10^{15}$ Hz ($\sim$4 eV), which is determined by the wind temperature.

The effects of the stellar wind parameters (i.e. mass-loss and terminal velocity) on the combined radio spectra of the system are illustrated in Figs 3 and 4 for $L_{\rm X} = 10^{37}$ and 10^{39} erg s^{-1}, respectively. Two characteristic observing radio frequencies are indicated with vertical dashed lines. Within the figures, the spectral indices for radio frequencies are also noted. The competition between the thermal and non-thermal emission processes determines the observed radio spectrum. For instance, for a strong Be wind scenario as in model W3, and sufficiently low accretion rates, the radio luminosity at 6 and 22 GHz is dominated by the thermal wind emission (compare purple lines on the right-hand side panels in Figs 3 and 4).

Before closing this section, it would be useful to put the spectral predictions of our model into perspective. We therefore compare the thermal and non-thermal emission of our model for the default parameter values (Table 2) and the various wind models presented in Table 1 with the spectrum of a massive companion star and the X-ray emission powered by accretion. As a representative example, we used the Kurucz spectral model for a massive star with $T_{\rm eff} = 2.5 \times 10^4$ K, radius $5\,{\rm R}_\odot$, gravitational acceleration $\log g = 5$ (in cgs units), turbulent velocity $v_{\rm turb} = 2$ km s^{-1}, and solar composition.[5] X-rays are produced both in the accretion disc and in the accretion column above the NS surface. As an illustrative example, we considered the Becker & Wolff (2007) model that computes the spectrum of the accretion column. The model assumes a cylindrically collimated radiation-dominated radiative shock in the accretion flow confined by the NS magnetic field and has been applied to prototypical X-ray pulsar Her X−1 (Wolff et al. 2016). For the accretion column spectrum, we used $B = 10^{12}$ G and $\dot{M} = 10^{18}$ g s^{-1}, while the rest physical parameters where fixed to their typical values (Wolff et al. 2016). The spectrum of the accretion disc is approximated by a multitemperature blackbody with an inner disc radius $R_{\rm in} = R_{\rm M} \simeq$ 500 km and a temperature $T_{\rm in} = 0.1$ keV. Our results are presented in Fig. 5. Stellar radiation dominates the emission from near-infrared[6] (NIR) to optical/UV frequencies. This is a major difference with low-mass XRBs where the NIR/optical emission has contributions from the disc and the jet in low-hard states (e.g. Markoff et al. 2003; Russell

[5] https://wwwuser.oats.inaf.it/castelli/grids.html

[6] We neglected possible contribution of the decretion disc in this energy range.

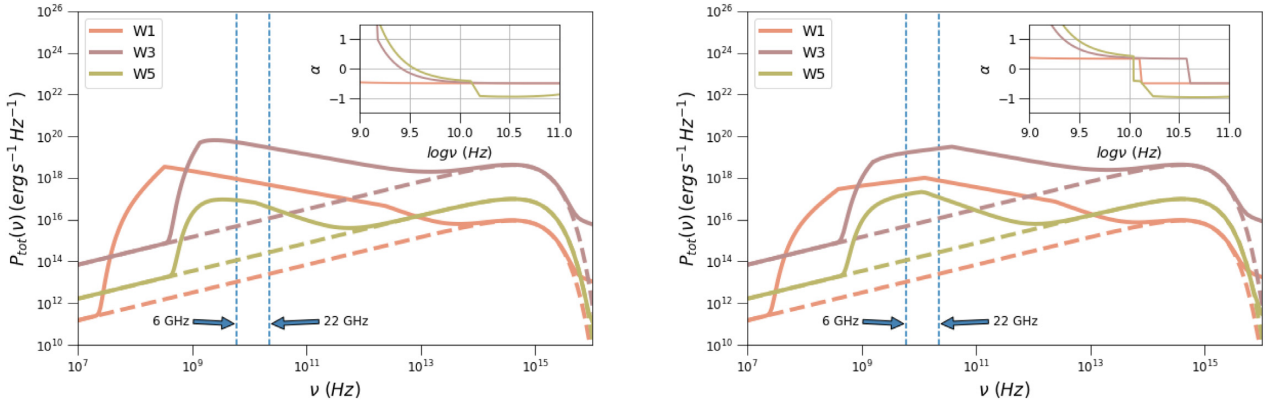

Figure 4. Same as in Fig. 3 but for $L_X = 10^{39}$ erg s^{-1}.

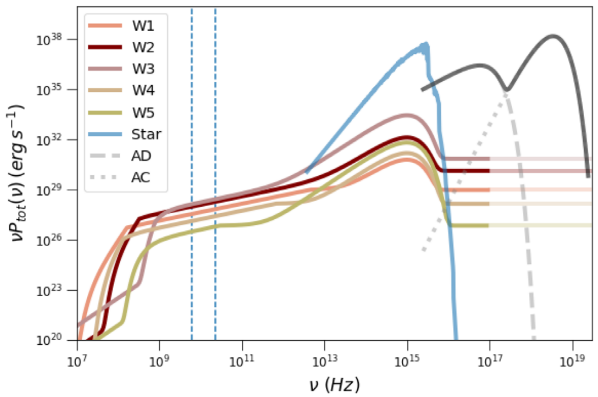

Figure 5. Composite radio-to-X-ray spectra for a fiducial HMXB with $L_X = L_{Edd} = 1.8 \times 10^{38}$ erg s^{-1}. The spectrum from the stellar surface of the massive companion is overplotted with solid blue line. The X-ray spectra (without absorption) from the accretion column (AC, dotted grey line) and the accretion disc (AD, dashed grey line) are also shown for comparison purposes. Vertical dashed lines mark the 6 and 22 GHz frequencies.

et al. 2013). The synchrotron spectrum of relativistic electrons in the WCR can extend to X-rays (transparent solid coloured lines) for sufficiently high γ_{max} values. Here, γ_{max} is computed by balancing the synchrotron loss rate with the acceleration rate (in the Bohm limit). Hence, the spectrum extends to ∼160 MeV, known as the synchrotron burn-off limit (de Jager et al. 1996). IC cooling is not included in the determination of γ_{max} because scatterings of stellar photons by electrons with such high Lorentz factors happen deep in the Klein–Nishina regime. Even though synchrotron emission is guaranteed in the X-ray regime, its luminosity is orders of magnitude smaller than the X-ray luminosity from the accretion column and the inner regions of the accretion disc.

3.2 The L_R–L_X diagram

Examining our model predictions for the emission at 6 GHz for a wide range of X-ray luminosities, we can construct the L_R versus L_X plot, as shown in Fig. 6 for two values of the binary separation distance. In all cases considered, there is a range of X-ray luminosities where the free–free emission from the Be wind dominates; hence, $L_R \propto L_X^0$. For higher X-ray luminosities, a power-law relation is established, i.e. $L_R \sim L_X^b$ with $b \simeq 1.7$–1.8. In this regime, the 6 GHz luminosity is attributed to the optically thin part of the (uncooled) synchrotron spectrum (see also left-hand side panels in Figs 3 and 4). For even higher values of L_X, we still find a positive correlation between radio and X-ray luminosities, but with $b \sim 0.3$, as shown in the left-hand side panel of Fig. 6.

The change in slope b signals a change in the wrapping orientation of the WCR; i.e. the shock is wrapped around the NS for low enough L_X ($\eta > 1$), but then is pushed towards the Be star as the accretion rates become higher ($\eta < 1$). The value of L_X that corresponds to this transition is found by setting $\eta = 1$ (see equation 4)

$$L_{X,\rm br} \simeq 4 \times 10^{37}\, \epsilon_{-1}\, \xi_{-0.3}^{7/16}\, \mu_{\rm NS,30}^{1/4} M_{\rm NS,0.15}^{-1/2} \left(\frac{\dot{M}_{\rm Be,-9} V_{\rm Be,3}^{\infty}}{\eta_{\rm out,-1}\chi_0}\right)^{7/8} \text{erg s}^{-1}, \quad (14)$$

where $\mu_{NS} \equiv B_{NS} R_{NS}^3$ is the NS dipole magnetic moment. We also introduced the notation $q_x = q/10^x$, with the mass-loss rate in units of $M_\odot$ yr^{-1}, the wind velocity in units of km s^{-1}, and the NS mass in units of the solar mass. Note that for typical parameter values, the transition occurs close to the Eddington luminosity of a NS.

As long as the radio frequency of interest falls in the optically thin (and uncooled) part of the synchrotron spectrum, the relation $L_R \propto L_X^b$ can be derived analytically, as shown in Appendix B,

$$L_R \propto \begin{cases} L_X^{12/7}, & \eta \gg 1 \text{ or } L_X \ll L_{X,\rm br} \\ L_X^{2(p-1)/7}, & \eta \ll 1 \text{ or } L_X \gg L_{X,\rm br}. \end{cases} \quad (15)$$

For the dependences of L_R on the model parameters, we refer the reader to Appendix B.

Similar results are found for smaller binary separation distances, as shown in the right-hand panel of Fig. 6. However, as the system becomes more compact, the shallow part of the radio X-ray luminosity curve (with $b \sim 0.3$) becomes truncated due to the increasing role of absorption. In other words, the abrupt steepening indicates that the radio emission at 6 GHz becomes optically thick. Moreover, for high enough L_X values (depending on the wind model) the WCR is pushed very close to the Be star, making these solutions not physically meaningful (dashed coloured lines). Note also that for weak Be winds (like in model W5) and high X-ray luminosities (i.e. strong NS outflows), GHz-emitting electrons can be fast cooling due to strong IC losses (black dotted lines).

3.3 Effects of model parameters

The impact of the main model parameters on the L_R–L_X diagram is illustrated in Fig. 7. In each panel, we vary one model parameter as

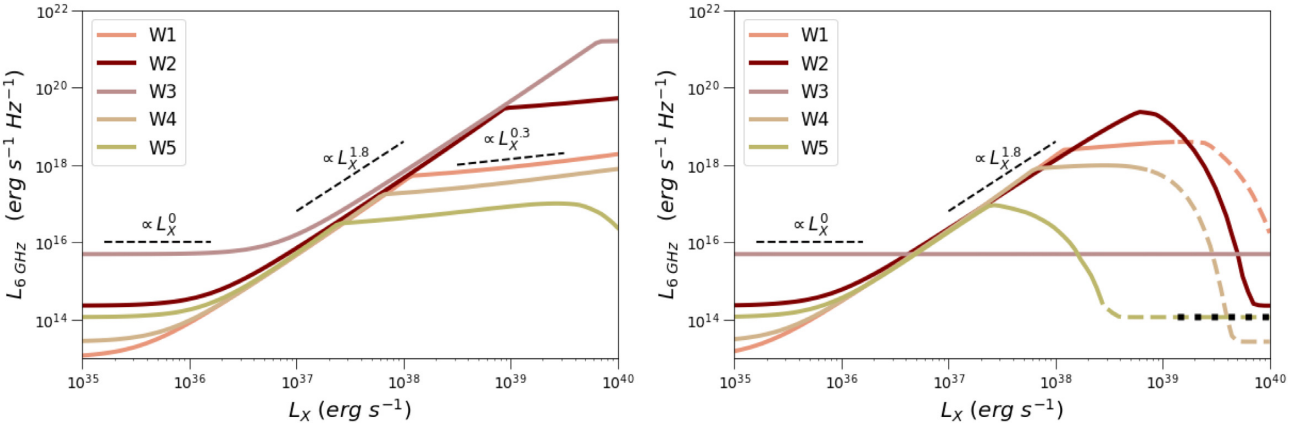

Figure 6. Luminosity at 6 GHz plotted against the X-ray luminosity due to accretion for the wind models presented in Table 1. Left- and right-hand panels show results for $D = 1000$ and 100 $R_\odot$, respectively. Dashed lines represent non-physical solutions with $R_{sh} < 20$ $R_\odot$. Dotted black lines correspond to the fast electron cooling regime where our analysis is not valid. For strong stellar winds, like in W3, the emission can be dominated by the wind thermal radiation, which is independent of the NS X-ray luminosity (see right-hand panel).

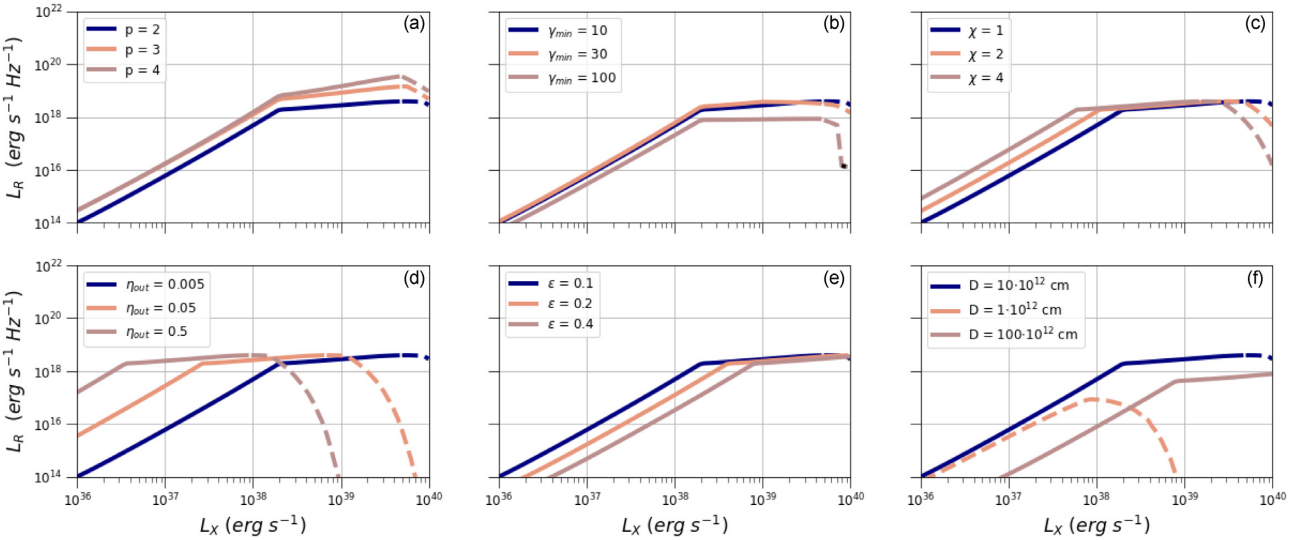

Figure 7. Impact of the model parameters on the L_R–L_X diagram for the W1 model: (a) power-law slope electron distribution, (b) minimum Lorentz frequency of the electron distribution, (c) deviation of the NS outflow velocity from the Keplerian value at the inner disc radius, (d) fraction of the NS accretion rate that gets lost through outflow, (e) mass-to-energy conversion efficiency of the accreting NS, and (f) the binary distance. In all panels, dashed lines represent non-physical solutions with $R_{sh} \leq 20$ $R_\odot$. Dotted black lines correspond to the fast electron cooling regime where our analysis is not valid.

indicated in the inset legends, while keeping the others fixed to the following values: $p = 2$, $\gamma_{min} = 3$, $\chi = 1$, $\eta_{out} = 0.005$, $\epsilon = 0.1$, and $D = 10^{13}$ cm. Here, the wind model W1 is used.

Examining the different panels of Fig. 7, we can make the following remarks. First, a steeper power-law distribution in electrons (panel a) implies a larger number of accelerated electrons at lower energies. Hence, the number of particles radiating at radio frequencies is larger for $p = 4$ than for $p = 2$, when all other parameters are fixed, and an increase in L_R is found. Notice also the change in slope b of the power-law segment above the critical X-ray luminosity (see also equations 14 and 15). The synchrotron luminosity at 6 GHz also depends on the chosen value of γ_{min} (panel b). For higher values of γ_{min}, the optically thin synchrotron emission at a fixed frequency (here, 6 GHz) decreases due to the smaller number of low-energy electrons radiating at that frequency. For the same physical conditions, the electron cooling Lorentz factor (see equation 6) can be smaller than γ_{min}, if the latter is sufficiently large (dotted black lines for $\gamma_{min} = 100$). The acceleration of the NS outflow to a speed χ times larger than the Keplerian velocity at the inner disc radius does not affect much the shape of the L_R–L_X curve (panel c). Instead, an increase of χ directly implies a decrease in η (equation 4). Therefore, the whole curve shifts to the left with increasing χ. Similarly, the curves shift to the left and to the right with increasing η_{out} and decreasing ϵ, respectively (panels d and e). The binary separation distance has the biggest effect on the curves, as shown in panel f. For compact enough binaries, free–free attenuation by the stellar wind becomes very strong, thus reducing the 6 GHz radio luminosity. At the same time, the WCR can form very close to Be star, where the assumption for wind acceleration to terminal velocity breaks down.

Inspection of Fig. 7 shows that the radio luminosity computed at $L_{X,br}$ can be used as a proxy of the maximum expected value from an XRB (but see also panel a). This is independent of the parameters describing the NS outflow, namely χ, η_{out}, and ϵ, as shown in panels

c–e. Indeed, using equations (14) and (B5) we find

$$\nu_{\rm R} L_{\rm R}|_{L_{\rm X,br}} \simeq 2\times10^{27}\nu_{\rm R,10}^{\frac{1}{2}}\left(\dot{M}_{\rm Be,-9}V_{\rm Be,3}^{\infty}\right)^{\frac{7}{4}}\epsilon_{\rm B,-0.3}^{\frac{3}{4}} \epsilon_{\rm e,-0.3}D_{13}^{-\frac{1}{2}}\ \ln^{-1}\left(\frac{\gamma_{\rm max}}{\gamma_{\rm min}}\right)\ {\rm erg\ s^{-1}}, \quad (16)$$

where we assumed $p = 2$ for simplicity. Thus, the maximum radio luminosity at GHz frequencies depends mostly on the stellar wind momentum and the binary separation distance, and can range between 10^{27} and 10^{28} erg s^{-1} for typical parameter values. Interestingly, the maximum luminosity detected at 6 GHz in two XRBs with highly magnetized NSs is $\sim10^{28}$ erg s^{-1} regardless of the NS spin and magnetic field (van den Eijnden et al. 2021).

4 APPLICATION TO J0243

J0243 was the first Galactic source that exceeded by a factor of 10 the Eddington limit for a NS (Wilson-Hodge et al. 2018). It was therefore classified as a transient ULXP (for a review, see Kaaret et al. 2017). Its high luminosity and proximity made the source an ideal target for multiwavelength monitoring, resulting in the first detection of radio emission from a BeXRB during an outburst (van den Eijnden et al. 2018c).

Gaia parallax measurements of J0243 indicate that the source is located at a minimum distance of 5 kpc (van den Eijnden et al. 2018c). We therefore conservatively adopt this lower limit on the distance in our analysis. J0243 has an almost circular orbit with an orbital period of $\simeq$27.6 d and projected semimajor axis $a_* \simeq 3.5\times10^{12}$ cm (Wilson-Hodge et al. 2018).

The system was observed at radio frequencies (at 4.5, 6, 7.5, and 22 GHz) at multiple epochs that covered a wide range of X-ray luminosities. Here, we adopt the 6 and 22 GHz flux measurements of the system from van den Eijnden et al. (2018a, c). Whenever observations were performed at 4.5 and 7.5 GHz and a flat spectrum (i.e. $\alpha \approx 0$) was measured, then these fluxes were reported as representative of the 6 GHz flux (van den Eijnden et al. 2018a, c). The aforementioned papers also provide the 0.5–10 keV energy flux at multiple epochs. To convert the latter flux to a bolometric X-ray flux, we adopt a bolometric correction factor $K_{\rm bol} \equiv F_{\rm bol}/F_{0.5-10\,{\rm keV}} \approx 2.6$ from Tsygankov et al. (2018). Henceforth, we define periods with sub-Eddington and super-Eddington X-ray luminosities as epochs A and B, respectively. For completeness, the observed radio and X-ray luminosities for both epochs are listed in Table 3.

We then compare our toy model to the joint radio data (6 and 22 GHz) of each epoch separately. For the application to the data, we will employ a Bayesian approach to ensure accurately estimated model parameters and their associated uncertainties. Our goal is to infer the posterior probability density p given a data set ($\mathcal{D}$) and priors from the Bayes' theorem for a model with a set of parameters contained in the vector θ. Having calculated the model, we construct a likelihood function that can be defined as

$$\ln\mathcal{L}_i(\theta|\mathcal{D}_i) = -\frac{1}{2}\sum_k\sum_j \frac{\left(f^k_{\rm model,j} - f^k_{\rm data,j}\right)^2}{\left(\delta f^k_{\rm data,j}\right)^2}, \quad (17)$$

where $f_{\rm model,j}$ is the model radio flux at date j, $f_{\rm data,j}$ is the corresponding observed flux, $\delta f_{\rm data,j}$ is the associated error, and the index k runs over the different observing frequencies (here, 6 and 22 GHz).

We then derive posterior probability distributions for the model parameters and the Bayesian evidence with the nested sampling Monte Carlo algorithm MLFriends (Buchner 2014, 2019) using the UltraNest[7] package (Buchner 2021).

Table 3. Radio and X-ray luminosities of J0243.

Date (MJD)	$L_{\rm X}$ (10^{37} erg s^{-1})	$L_{6\,\rm GHz}$ (10^{28} erg s^{-1})	$L_{22\,\rm GHz}$ (10^{28} erg s^{-1})
	Epoch A (sub-Eddington)		
58170	1.03 ± 0.02	1.79 ± 0.06	–
58186	0.47 ± 0.02	0.44 ± 0.07	<0.76
58235	0.058 ± 0.003	<0.25	–
58239	0.43 ± 0.09	<0.27	–
58242	0.78 ± 0.15	1.17 ± 0.11	–
58249	1.5 ± 0.2	1.20 ± 0.12	–
58259	0.39 ± 0.08	<0.24	–
	Epoch B (super-Eddington)		
58036	11.12 ± 0.08	<0.2	<0.6
58065	287.0 ± 1.9	1.38 ± 0.08	–
58072	184.3 ± 1.2	1.66 ± 0.07	2.6 ± 0.3
58078	124.4 ± 0.9	1.14 ± 0.08	1.9 ± 0.4
58079	110.4 ± 0.8	0.99 ± 0.08	2.0 ± 0.5
58085	81.7 ± 0.5	0.62 ± 0.07	2.0 ± 0.3
58089	50.3 ± 0.3	0.44 ± 0.08	1.8 ± 0.3
58127	12.75 ± 0.08	0.38 ± 0.07	–

Notes. Errors and upper limits are 1σ and 3σ, respectively. Data are adopted from van den Eijnden et al. (2018a, c).

During this procedure, we fix $B_{\rm NS} = 10^{12}$ G, $R_{\rm NS} = 10$ km, $M_{\rm NS} = 1.4\ {\rm M}_\odot$, $\epsilon = 0.2$, $\chi = 2$, and $p = 2$. We adopt $L_{\rm Be} = 3\times10^4\ {\rm L}_\odot$ based on the spectral type of the companion star in J0243 (O9.5V; Reig, Fabregat & Alfonso-Garzón 2020). For all other parameters (a complete list can be found in Table 2), we assume uniform prior distributions over a wide range of values except for the binary separation distance, D. For the latter parameter, we consider a narrower range, i.e. $a_* \le D \le 2a_*$, as even larger D would imply a very massive companion ($\gtrsim$27 M$_\odot$) that can be excluded based on spectroscopic observations of the system Reig et al. (2020). We finally impose the constraints $\epsilon_{\rm e} = \epsilon_{\rm B}$ equipartition between relativistic particles and magnetic fields and $i = \sin^{-1}(a_*/D)$.

The $L_{\rm R}$–$L_{\rm X}$ diagram for epoch A and the two radio frequencies is presented in Fig. 8 (top and middle panels). The radio data in epoch A can be satisfactorily explained by the model. The large uncertainty in the 22 GHz flux for $L_{\rm X} \gtrsim 10^{37}$ erg s^{-1} is also reflected to the spread in the values of the predicted spectral index in the 6–22 GHz range (see bottom panel in Fig. 8). The observational values are computed assuming a power-law spectrum between two frequencies of reference. We adopt a similar approach when deriving the indices plotted in the figure, since the spectrum can be well described by a power law in the narrow range of 6 and 22 GHz most of the times (see e.g. inset plots in Fig. 3). Because of the large uncertainties in the observational values of α, a shock origin of the radio data (with $\alpha \le 0$) cannot be excluded at the 3σ level as shown in Fig. 8, in contrast to what has been argued by van den Eijnden et al. (2018a).

The corresponding corner plot with the posterior probability distributions of the model parameters is shown in Fig. C1. The radio data of epoch A can be described well by the model for reasonable wind parameters ($\dot{M}_{\rm Be} \simeq 3\times10^{-9}$ M$_\odot$ yr^{-1} and $V_{\rm Be}^{\infty} \simeq 1260$ km s^{-1}), if about 16 per cent of the accreted material to the NS is lost through outflows (see Fig. C1). Moreover, the minimum electron Lorentz factor and the fraction of shocked fluid energy transferred to particles and magnetic fields are well constrained (i.e. $\gamma_{\rm min} \approx 16$ and $\epsilon_{\rm B} \simeq 0.5$). The true binary separation distance is, however, not well determined as illustrated by the posterior distribution

[7] https://johannesbuchner.github.io/UltraNest/

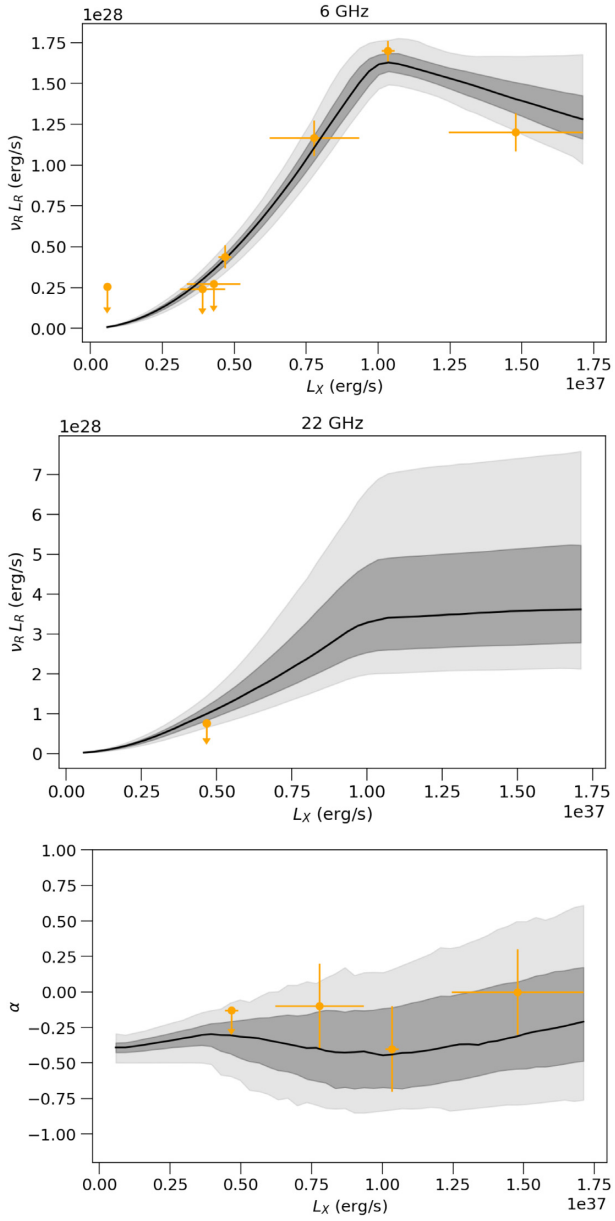

Figure 8. *Top and middle panels:* Model fits to the 6 and 22 GHz radio luminosities during epoch A. Dark and light shaded regions indicate the 68 and 99 per cent confidence intervals, respectively. *Bottom panel:* Spectral index α between 6 and 22 GHz obtained from our model fit. Measured spectral indices are shown with symbols (adopted from van den Eijnden et al. 2018a, c). Dark and light shaded regions indicate the 68 and 99 per cent confidence intervals, respectively.

that is approximately uniform (as the adopted prior distribution). We also performed the simulations with p being sampled from a uniform distribution between 2 and 4, but the power-law slope could not be constrained either. Hence, a more complex physical model where the particle injection spectrum would have had an angular dependence (e.g. softer further from the shock apex) would not be easily distinguished by a simpler one where p is constant using the existing data.

For completeness, we also show in Fig. 9 the model-predicted spectra for parameter values drawn from the posterior distributions for two different dates. Observational data are overplotted with

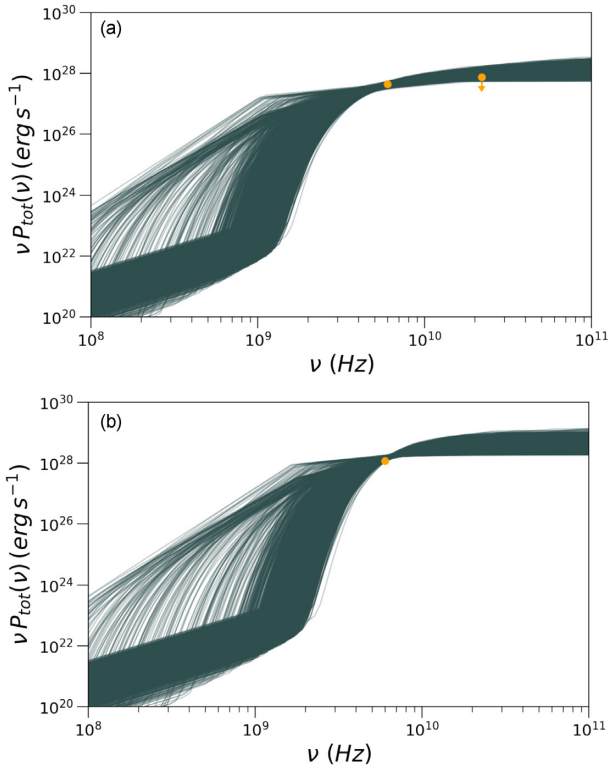

Figure 9. Radio spectra of J0243 computed using parameter values from the posterior distributions for two different dates from epoch A: 58186 MJD (panel a) and 58249 MJD (panel b).

symbols, whenever available (see also Table 3). Broadly speaking, we find that both observing radio frequencies fall into the optically thin part of the synchrotron spectrum, while the free–free emission of the stellar wind is always subdominant, in agreement with the estimates of van den Eijnden et al. (2018c).

Application of the model to epoch B shows that the posterior probability distributions do not differ much (within 1σ) from those of epoch A, except for $\dot{M}_{\rm Be}$ and $V_{\rm Be}^{\infty}$ whose distributions shift to smaller and higher values, respectively (see Fig. C2). Moreover, the posterior distribution of the binary separation distance is not uniform as in epoch A, but shifted towards the upper end of the assumed range of values. In general, all posterior distributions are narrower than those in epoch A due to the larger number of observational constraints in epoch B. Our toy model can satisfactorily describe the data, as shown in the $L_{\rm R}$–$L_{\rm X}$ diagrams at 6 and 22 GHz and the spectral index plot (see Fig. 10). However, none of the displayed models is physically meaningful, as they predict the formation of the WCR at distances less than 20 $R_{\odot}$ from the Be star. In this regime, our assumption of a stellar wind moving with its terminal radial velocity breaks down. If the wind is moving with much lower speeds, then the formation of a strong shock might also be questionable.

5 DISCUSSION

We have presented a one-zone model for the radio emission from HMXB systems and computed the expected $L_{\rm R}$–$L_{\rm X}$ relation under several simplifying assumptions. In this section, we discuss some of these aspects and their possible impact on our results. We also discuss the findings of our toy model in light of recent radio observations of a sample of NS XRBs (van den Eijnden et al. 2021).

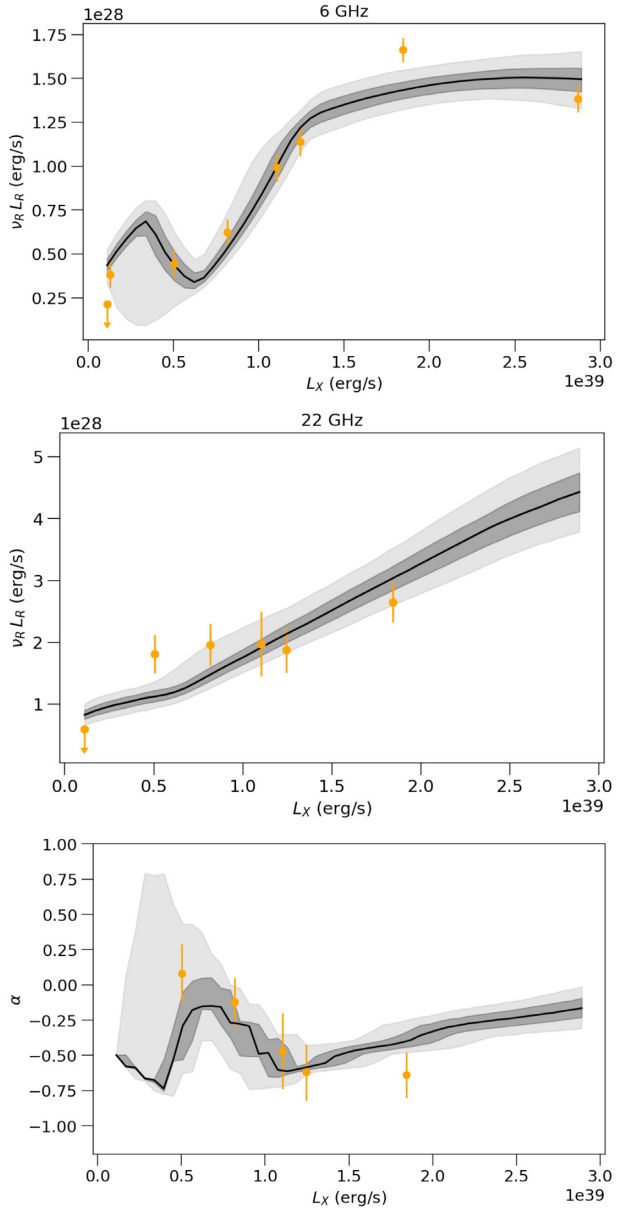

Figure 10. Same as in Fig. 8 but for epoch B. All of the displayed solutions lead, however, to non-physical solutions with $d_{\rm Be} < 20\,{\rm R}_\odot$.

5.1 High-energy emission

In our study, we have not discussed any potential signals of high-energy non-thermal radiation from HMXBs. The massive companion star is a source of low-energy radiation that can be up-scattered to high energies by the radio-emitting electrons in the WCR. In fact, for typical stellar luminosities and magnetic field strengths in the WCR, electrons lose energy through IC scattering more efficiently than synchrotron radiation (see also section 2.2). Electrons radiating at 10 GHz have Lorentz factors $\gamma_{\rm R} \sim 100$, assuming typical parameter values (i.e. $\dot{M}_{\rm Be} = 10^{-9}\,{\rm M}_\odot\ {\rm yr}^{-1}$, $V_{\rm Be}^{\infty} = 10^3$ km s^{-1}, $\epsilon_{\rm B} = 0.1$, $\eta_{\rm out} = 0.1$). These electrons can IC scatter stellar optical photons at X-ray energies. The ratio of IC and synchrotron luminosities produced by radio-emitting electrons can be approximately written as $(\nu L_\nu|_{\rm IC})/(\nu L_\nu|_{\rm syn}) \approx U_{\rm ph}/U_{\rm B} = 8L_{\rm Be}/(9c\,\epsilon_{\rm B}\dot{M}_{\rm Be}V_{\rm Be}^{\infty}) \simeq 1800\,L_{\rm Be,4}\epsilon_{\rm B,-1}^{-1}\dot{M}_{\rm Be,-9}^{-1}(V_{\rm Be,3}^{\infty})^{-1}$, where $L_{\rm Be,4} = 10^4\,{\rm L}_\odot$ and Thomson scattering was assumed. The only two HMXBs hosting strongly magnetized NSs have GHz radio luminosities $\sim 10^{28}$ erg s^{-1} (van den Eijnden et al. 2021). Assuming that their radio emission is powered by synchrotron radiation from the WCR, the predicted X-ray luminosity due to IC scattering cannot be much higher than $\sim 10^{32}$ erg s^{-1}. This prediction is still many orders of magnitude below the X-ray luminosity produced via accretion on to the NS; hence, it cannot be used as a probe of the physical conditions in the radio-production site of the system. The IC scattered emission can extend and actually peak (in νL_ν units) in the gamma-ray band, as shown for colliding-wind binary systems (e.g. Reimer, Pohl & Reimer 2006; Werner et al. 2013; Pittard et al. 2021). Even though many of these systems have been observed in radio wavelengths (for a catalogue, see De Becker & Raucq 2013), the predicted non-thermal high-energy emission in X-rays and gamma-rays remains elusive. So far, non-thermal X-rays and TeV gamma-rays have been detected only from η Carinae (Hamaguchi et al. 2018; H. E. S. S. Collaboration 2020). Detailed radiative models for high-energy emission from colliding-wind binaries show that the GeV gamma-ray luminosity from IC scattering can be up to 10^2–10^4 times higher than the GHz radio luminosity, depending on the binary separation distance and the orbital phase (e.g. Pittard et al. 2021). Similar ratios can be expected in our scenario, as it bears many similarities with the shock-wind models for massive binaries. However, due to the lower radio luminosities of HMXBs with magnetized NSs (van den Eijnden et al. 2021) any gamma-ray signal would be even more difficult to detect than in massive binaries.

5.2 Simplifying assumptions

In our analysis, we considered $\eta_{\rm out}$ constant, but in principle it can depend on the accretion rate on to the NS. For instance, if the NS outflows are driven by changes in the disc structure as the accretion rate increases, then one would expect $\eta_{\rm out} \ll 1$ for $L_{\rm X} \ll L_{\rm Edd}$ and $\eta_{\rm out} \sim 0.1$–0.5 otherwise (e.g. Mushtukov et al. 2019). How would such an $L_{\rm X}$-dependent outflow fraction change the $L_{\rm R}$–$L_{\rm X}$ diagram? This can be qualitatively understood by looking at panel d in Fig. 7. A decrease in $\eta_{\rm out}$ would not affect the maximum predicted radio luminosity, but would require higher $L_{\rm X}$ values in order to achieve it. If the outflow fraction changed from 0.005 to 0.5 at $L_{\rm X} \sim 10^{38}$ erg s^{-1}, then the $L_{\rm R}$–$L_{\rm X}$ diagram would be the combination of the blue and brown coloured curves. In this scenario, it is therefore not possible to explain similar radio luminosities for sub-Eddington and super-Eddington X-ray luminosities, as observed in J0243 (van den Eijnden et al. 2018b). On the contrary, we found that an almost constant outflow fraction $\eta_{\rm out}$ and a variable Be stellar wind could broadly describe the multi-epoch observations of J0243 (see e.g. Figs C1 and C2).

Effects on the structure of the WCR due to the orbital motion were not taken into account. If the orbital velocity is sufficiently large (i.e. close binaries), then the WCR would wrap around the stars because of the Coriolis forces acting upon it. The structure of the WCR in the orbital plane would look like a spiral (e.g. Lemaster, Stone & Gardiner 2007; Parkin & Pittard 2008; Johnstone et al. 2015; Rodríguez et al. 2020). Hence, the line of sight would cut through more regions containing non-thermal particles. If the radio-emitting electrons that are injected into the WCR close to the apex do not suffer strong energy losses as they stream to the more distant regions of the WCR, then they could contribute to the synchrotron radio luminosity of the system. An orbital modulation of the radio flux would be expected in this case. The ratio of the orbital velocity to the wind speed is a useful estimator of the importance of orbital motion effects (Lemaster et al. 2007). Assuming an almost circular orbit, like

in J0243, the ratio reads $V_{\rm orb}/V_{\rm Be}^{\infty} = \sqrt{G(M_{\rm NS}+M_{\rm Be})/D}/V_{\rm Be}^{\infty} \simeq 0.06\,(D/10^3\,{\rm R}_{\odot})^{1/2}(V_{\rm Be}^{\infty}/10^3\,{\rm km\,s^{-1}})^{-1}$, where a 20 $M_{\odot}$ companion star was assumed. Thus, for typical parameters used in this study, orbital effects should not affect the shape of the WCR.

In this proof-of-concept work, we adopted a one-zone toy model for the calculation of the synchrotron radiation from the WCR. We assumed that all physical quantities (e.g. post-flow velocity, post-shock energy density, electron power-law slope, and others) remain constant in the emitting volume, having values equal to those computed at the shock apex. Because the shape and properties of WCR change at large angles from the line of centres (e.g. Pittard, Vila & Romero 2020), we limited our calculations to a spherical wedge with opening angle $\pi/4$ (with respect to the line of centres), corresponding to a volume $\pi {\rm R}_{\rm sh}^3$. A more accurate calculation would require a multizone radiation model that follows the particle distribution along the streamlines of the post-shock fluids, taking into account radiative and adiabatic energy losses (e.g. del Palacio et al. 2016; de la Cita et al. 2017; van der Merwe et al. 2020; Pittard et al. 2021). Such multizone models can also account for potential changes in the particle injection spectrum (e.g. power-law slope and accelerated energy fraction) as a function of angle due to changes in the shock obliquity and Mach number (see Pittard et al. 2021, and references therein). Angular dependence in the physical parameters of the model would generally lead to smoother synchrotron spectra than those presented here, unless the total spectrum is dominated by particles within a small range of angles (see e.g. fig. 3 of del Palacio et al. 2016). Another effect that cannot be captured by a one-zone model for radio emission is that the free–free opacity may vary along the line of sight, if the synchrotron-emitting region is physically extended, as observed in certain radio-emitting colliding-wind binaries (see Dougherty et al. 2003, and references therein). Nevertheless, the one-zone emitter may still be a good approximation for NS XRBs, like J0243, that are detected as point sources in radio frequencies (van den Eijnden et al. 2018b, c). In fact, J0243 is about 10 times more distant with $\sim 10^{-3}$ times lower flux in GHz frequencies than WR 147, a well-studied colliding-wind massive binary system with resolved radio emission (e.g. Watson et al. 2002; Dougherty et al. 2003; Reig et al. 2020).

5.3 Interpretation of modelling results of Swift J0243.6+6124

Using a Bayesian approach, we searched for model parameters that describe the data of J0243 at 6 and 22 GHz over a wide range of X-ray luminosities, and found that our toy model can describe reasonably well the data. The posterior distributions of the model parameters found for epoch A are physically meaningful. No significant changes in the model parameters were required for explaining the data of epoch B except for the properties of the stellar wind: The mass-loss rate decreased by a factor of $\sim$25, while its terminal velocity increased by a factor of $\sim$4 (see Figs C1 and C2). These values result in a lower wind momentum, which when combined with the higher X-ray luminosities, translate to a very weak stellar wind. If accretion on to the NS took place through the wind, then the combination of the above-mentioned effects should reduce the mass accretion rate on to the NS. It would be then difficult to explain the high accretion rates sustained for $\sim$3 month period in epoch B. However, in BeXRBs mass transfer is due to interactions of the NS with the Be disc, a mechanism that seems to hold even in major outbursts that last for several orbital periods (e.g. Martin et al. 2014). Thus, the NS can accrete material that has been already captured by the NS at a prior time, and a WCR forms because of the NS outflow colliding with the stellar wind. To better understand the dynamics of this complex system of accretion inflow/outflow and stellar wind/disc, three-dimensional relativistic (magneto-)hydrodynamical simulations should be performed.

The derived stellar wind properties for epoch B are also in tension with theoretical and numerical studies of hot stellar winds (e.g. Fransson & Fabian 1980; Blondin 1994; Krtička et al. 2015). For high enough X-ray luminosities, the gas that resides on the stellar surface exposed to the X-ray source becomes highly photoionized, thus suppressing the wind velocity or even halting the formation of a radiatively driven wind from that side. The effect of the X-rays on the stellar wind is expected to be stronger for larger X-ray luminosities, lower mass-loss rates, and faster winds (e.g. Krtička et al. 2015), as found for epoch B. More recently, Krtička, Kubát & Krtičková (2018) showed that clumping of the Be stellar wind in the radial direction can weaken the effects of X-ray irradiation because of the balancing effect of recombination. Even if clumpiness is not taken into account, stellar wind can still escape from the other side of the star, causing the so-called shadow wind that is often seen in luminous HMXBs (as in e.g. 4U 1700−37; Haberl, White & Kallman 1989). In fact, the shadow wind model (Blondin 1994) has been offered as a possible mechanism to explain periodic dips (on orbital time-scales) seen in the ULXP M51 ULX−7 (Vasilopoulos et al. 2021) and in SMC X−2 during its 2015 super-Eddington outburst (Li et al. 2016). Summarizing, X-ray emission from the compact object can lead to anisotropic and inhomogeneous stellar winds. However, these effects on the WCR emission are beyond the scope of this work.

5.4 Jets in HMXBs?

We demonstrated that a shock origin of the radio emission of J0243 for $L_{\rm X} < L_{\rm Edd}$ is possible with reasonable parameter values, while it is disfavoured for the super-Eddington accretion phase of the outburst based on physical arguments. Still, the flat radio spectrum ($\alpha \leq 0$) observed in this phase (see Fig. 10) implies the presence of non-thermal emitting particles. This raises the question of where these particles could be found besides the WCR. While radio-emitting jets (i.e. collimated outflows) are ubiquitous in low-mass XRBs with weakly magnetized NSs ($B_{\rm NS} \leq 10^9$ G), they have not been unambiguously identified in HMXBs with strongly magnetized NSs. The lack of solid observational evidence for the presence of jets in combination with the incomplete theoretical understanding of jet launching in such systems makes the interpretation of data within the jet scenario dubious. For instance, Kylafis et al. (2012) argued that no compact jet can be formed in accreting NSs with $B_{\rm NS} \gtrsim 10^{12}$ G, because the physical mechanism producing large-scale magnetic fields in the disc needed for the jet formation cannot operate efficiently. Massi & Kaufman Bernadó (2008) also argued that no jet can form in accreting NSs with $B_{\rm NS} > 10^{12}$ G because the strong magnetic field cannot be twisted, as it is always dynamically important (compared to the gas in the inner disc). Alternatively, a jet could be formed by collimating the pulsar wind moving along opened field lines. Collimation, which could be mediated by external large-scale magnetic fields or by the pressure of dense plasma (e.g. from disc winds), would be necessary to make the pulsar wind appear as a typical radio jet, as in their large-scale analogues in active galaxies (e.g. Tchekhovskoy, Narayan & McKinney 2011; Vlahakis 2015; Boccardi et al. 2021). Recently, Parfrey et al. (2016) studied the disc-induced opening of magnetic field lines in accreting millisecond pulsars, and derived a measure of the power carried by the pulsar wind as a function of the mass accretion rate on to the NS, namely

$L_j \propto \dot{M}^{4/7}$. While this does not relate directly the radio luminosity, which depends on the uncertain nature and location of the dissipation mechanism in the jet as well as the jet bulk motion, with L_X it is useful for our qualitative discussion. Given that radiation-driven outflows from the disc are expected for super-Eddington accretion rates (Shakura & Sunyaev 1973; Poutanen et al. 2007; Campana et al. 2018), the required collimation of the pulsar wind might be possible in J0243 for $L_X > L_{Edd}$. In epoch A ($L_X < L_{Edd}$), the much lower accretion rates would power a weaker jet even if the collimation was still present. Hence, a hybrid scenario where the radio emission is dominated by the WCR at sub-Eddington X-ray luminosities and by a collimated outflow (jet) at super-Eddington luminosities is plausible.

The collimated pulsar wind model of Parfrey et al. (2016) was also discussed in the light of recent radio observations of HMXBs with strongly magnetized NSs (van den Eijnden et al. 2021). These authors found no correlation between radio and X-ray luminosity for the sources in the sample (and for J0243 individually) in contrast to the scaling $L_j \propto \dot{M}^{4/7}$. Moreover, the radio luminosity of the sources in the sample did not seem to depend on the NS magnetic field and/or spin, as theoretically predicted. These findings imply that either the jet power and radio luminosity have a complicated relation that depends on the accretion rate or that more than one radio production region might be at work in HMXBs with strongly magnetized NSs.

5.5 Potential diagnostics for the radio origin

The above discussions raise an interesting question: Would it be possible to discriminate between a jet and a shock origin for the radio emission in HMXBs? Potential diagnostics include the (i) radio/X-ray correlation, (ii) radio/NIR/optical polarization, (iii) orbital modulation of radio fluxes, and (iv) radio-to-NIR spectral shape. For the sake of argument, let us assume that a compact steady jet can be formed in XRBs with highly magnetized NSs as in the low-hard states of BH XRBs. We can therefore compare our model predictions with those of well-tested jet models for the low-hard states of BH XRBs (e.g. Heinz & Sunyaev 2003; Merloni et al. 2003).

(i) Even though our model makes clear predictions about the radio/X-ray correlation (see e.g. equation 15 and Figs 6–7), similar shapes can be obtained in the context of compact jet models. For instance, jet models accounting for both the radio and X-ray emissions in BH XRBs predict $L_R \propto L_X^{1.4}$ for a wide range of $L_X < L_{Edd}$ (e.g. Markoff et al. 2003). Depending on the stellar wind properties, observations of HMXBs could capture only the steep branch of the correlation in our scenario, which has a similar slope ($L_R \propto L_X^{1.7}$). Only through quasi-simultaneous radio/X-ray observations of individual systems mapping a wide range of mass accretion rates up to the Eddington limit, as in J0243, would be possible to critically test the jet and shock models for radio emission.

(ii) Radio polarization might be not ideal for distinguishing between a jet and shock origin of the radio emission. In both cases, radio is produced by synchrotron radiation, whose polarization degree (PD) depends on the magnetic field geometry and properties of the external medium. In both models, there is a degree of freedom in regard to the magnetic field configuration in the emission region. For instance, a low PD in a jet scenario would be expected if the plasma is turbulent in the radio emitting region, while a higher PD would be expected if the magnetic field is predominantly toroidal, as is theoretically predicted in the inner regions of magnetically dominated jets (e.g. Meier, Koide & Uchida 2001; Vlahakis & Königl 2004). Similarly, in the WCR the magnetic field will depend on the binary separation distance, the magnetic field of the stellar wind, and the development of turbulence in the shock region (see Pittard et al. 2021, and references therein). Variable PDs are also expected in both scenarios, as they can be related to dynamical changes in the emission region. Synchrotron radiation on long wavelengths can also be depolarized by radiative transfer effects, such as Faraday rotation due to the thermal plasma of the stellar wind (Hales et al. 2017). As a result, a low or high PD cannot uniquely determine the origin of the radio emission. Meanwhile, polarization at NIR/optical frequencies cannot probe the non-thermal synchrotron emission in HMXBs, as it is dominated by the stellar radiation of the massive companion (see Fig. 5).

(iii) Orbital modulation of the radio fluxes produced in the WCR or jet can be caused by variable attenuation from the wind of the massive star. Orbital modulation effects will depend on the inclination angle, binary separation distance, and stellar wind properties (i.e. temperature, mass-loss rate, temperature, and clumpiness). Zdziarski (2012) presented analytical expressions for the modulation depth due to free–free absorption by an isothermal wind when radio emission takes place close to the jet base ($z_0 \to 0$) or far away ($z_0 \gg D$). This analysis can also be applied to our scenario, if we neglect the curvature of the WCR (see Fig. A1). Because we consider radio emission from a small spherical wedge of the WCR, the corresponding z_0 cannot be much larger than the separation distance. In a jet model, the radio spectrum is a superposition of emission from different distances along the jet (Blandford & Königl 1979), while in our model there is a single region producing the radio emission. Therefore, in a jet model a frequency-dependent modulation in flux is expected because of the different locations of radio production in addition to the frequency dependence of the free–free absorption. A more careful analysis of these effects in the shock scenario is worth pursuing. From an observational point of view, HMXBs with day-long orbital periods would be ideal for the search of orbital modulation effects, since the X-ray luminosity can be considered constant within a period (in contrast to J0243).

(iv) Perhaps the most straightforward way of testing the jet and shock scenarios for radio emission is the shape of the spectrum from radio to NIR frequencies. The radio spectrum of a compact jet usually shows a break close to NIR frequencies, above which it becomes optically thin (e.g. Russell et al. 2013). Below that frequency, the jet spectrum is $F_\nu \propto \nu^0$. The synchrotron self-absorbed part of the spectrum in a single-zone model like ours is $F_\nu \propto \nu^{2-2.5}$. Moreover, the transition to optically thin emission takes place usually at lower frequencies (0.1–10 GHz) than in the standard jet model – see e.g. Figs 2–4. Quasi-simultaneous observations of individual systems performed over a wide range of frequencies (∼0.1 GHz to ∼100 THz) would be important for identifying potential spectral breaks in the spectrum.

5.6 Our results in a broader context

As this is, to the best of our knowledge, the first quantitative study of radio emission from such systems, we summarize our predictions on the radio–X-ray luminosity plane for XRBs (adopted from van den Eijnden et al. 2021). With coloured filled symbols are indicated HMXBs with strongly magnetized NS, including J0243 (green squares) and GX 1+4 (red squares). The dark and light shaded regions show the 68 and 99 per cent range of our model predictions for 10 000 samples drawn randomly from the following uniform

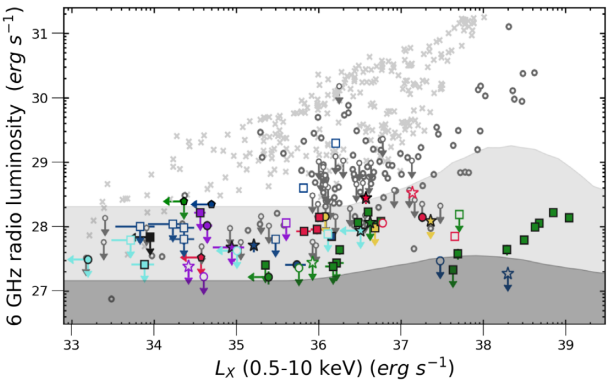

Figure 11. The L_R–L_X plane for XRBs. Figure adopted from van den Eijnden et al. (2021). Archival observations are shown in grey (crosses: black holes, circles: weakly magnetized NSs). Coloured symbols show recent observations of NS XRBs (filled markers: strongly magnetized NSs, open markers: weakly magnetized NSs). The borders of the dark and light shaded regions mark, respectively, the 80th and 99th percentiles of our solutions (the full bands are not shown).

distributions[8]: $\log \dot{M}_{\rm Be}(\mathrm{M}_\odot\ \mathrm{yr}^{-1}) \in [-9, -6]$, $\log (V_{\rm Be}^{\infty})(\mathrm{km\ s}^{-1}) \in [2, 3.5]$, $\log \gamma_{\rm min} \in [0.2, 2.2]$, $\log (D)(\mathrm{R}_\odot) \in [2, 3]$, $\log (\eta_{\rm out}) \in [-2, -0.3]$, $\log (\epsilon_{\rm B}) \in [-3, 0]$. All other parameters are fixed to their values listed in Table 2. We also assumed the same bolometric correction factor as in J0243 (see Section 4) for estimating the 0.5–10 keV luminosity. While the exact shape of the bands will depend on the adopted distributions, the flat part for $L_X \lesssim 10^{36}$ erg s^{-1} implies that most solutions are dominated by the free–free emission of the wind in this range of X-ray luminosities. When all physical parameters are randomly combined, then most of our solutions result in very low radio luminosities, i.e. $\sim 10^{22}$–10^{24} erg s^{-1} (well outside the plotting range of Fig. 11), with the median being 10^{26} erg s^{-1}. To reach luminosities as high as 10^{28} erg s^{-1}, special parameter combinations are needed, as also suggested by our analysis in Section 3 (see also equation 14). The borders of the dark and light shaded regions mark, respectively, the 80th and 99th percentiles of our solutions, where most of the upper limits and detections of NS XRBs are found. This means that, if our model is correct, we are just seeing the tip of the iceberg.

6 SUMMARY AND CONCLUSIONS

We have presented a toy model for radio emission in HMXBs with strongly magnetized NSs. We postulated that material is lost in the form of outflows from the accreting NS. The NS outflow, moving at a speed comparable to the Keplerian velocity at the inner disc radius, collides with the stellar wind of the massive companion forming a WCR. Radio emission is then expected from the system as a result of synchrotron radiation by shock-accelerated electrons in the WCR and free–free emission of the stellar wind. We explored the relation between the GHz luminosity and the X-ray luminosity powered by accretion for different model parameters and applied the model to J0243, a unique BeXRB with multiple radio detections extending over a wide range in X-ray luminosities.

We generally find that the radio luminosity at GHz frequencies is written as $L_R \propto L_X^b$. No correlation with X-rays is expected ($b = 0$) when the radio luminosity is dominated by the thermal emission of the stellar wind. Typically, for sub-Eddington X-ray luminosities we predict a steep correlation ($b \sim 12/7$) and a more shallow one [$b = 2(p-1)/7$] for super-Eddington X-ray luminosities, where p is the power-law index of accelerated electrons. The exact transition happens at a critical X-ray luminosity, $L_{\rm X,br}$, which mostly depends on the momentum ratio of the two outflows. Finally, a very steep anticorrelation is expected when the free–free opacity at GHz radio frequencies is very high, which is more common for compact binaries. The maximum radio luminosity (when this is dominated by optically thin synchrotron emission) is independent of the NS properties, such as magnetic field, fraction of mass lost through outflows, and radiative efficiency of accreting material. It depends mostly on the stellar wind momentum, binary separation distance, and the minimum Lorentz factor of accelerated electrons.

When applied to J0243, the model provides a good description of radio data for sub-Eddington X-ray luminosities with reasonable physical parameters. While the model can also fit the observations in the super-Eddington phase of the outburst, the parameters needed cannot be physically justified. Moreover, the WCR is pushed so close to the companion star that several of our model assumptions break down. It is therefore plausible that the radio emission of J0243 is dominated by the WCR at sub-Eddington X-ray luminosities and by a collimated outflow (jet) at super-Eddington luminosities.

In conclusion, the multi-epoch observations of J0243 offer the first opportunity to quantitatively test theoretical scenarios for radio emission in HMXBs with strongly magnetized NSs and help us understand the coupling of disc winds and jets. Regular radio monitoring of J0243 and GX 1+4 during different levels of X-ray luminosity and searches for orbital modulation in radio fluxes might help us distinguish between different scenarios. Looking into the future, more sensitive instruments like ngVLA (with 10 times the sensitivity of JVLA and ALMA; Selina et al. 2018) might reveal a large number of HMXBs with strongly magnetized NSs, constrain the slope of the L_R–L_X relation, and put our model into test.

ACKNOWLEDGEMENTS

The authors would like to thank the anonymous referee for insightful comments on the manuscript, Dr. J. Buchner for his advice on the use of the ULTRANEST package and its implementation, and Prof. N. Kylafis for comments on the manuscript. MP would like to thank the Observatory of Strasbourg for its hospitality during her visit in which this paper was completed. MP acknowledges support from the MERAC Foundation through the project THRILL.

This research made use of Astropy,[9] a community-developed core PYTHON package for Astronomy (Astropy Collaboration 2013, 2018), and ULTRANEST software package,[10] for model-to-data comparison using nested sampling (Buchner 2021).

DATA AVAILABILITY

Data used in this work are publicly available through published papers (van den Eijnden et al. 2018b, c, 2021).

REFERENCES

Abarca D., Parfrey K., Kluźniak W., 2021, ApJ, 917, L31

[8]We have not excluded the non-physical solutions that might exist above a certain L_X for different parameter values.

[9]http://www.astropy.org
[10]https://johannesbuchner.github.io/UltraNest/

Abbott D. C., Beiging J. H., Churchwell E., Torres A. V., 1986, ApJ, 303, 239
Astropy Collaboration, 2013, A&A, 558, A33
Astropy Collaboration, 2018, AJ, 156, 123
Basko M. M., Sunyaev R. A., 1976, MNRAS, 175, 395
Becker P. A., Wolff M. T., 2007, ApJ, 654, 435
Bell A. R., 1978, MNRAS, 182, 147
Blandford R. D., Königl A., 1979, ApJ, 232, 34
Blandford R. D., Ostriker J. P., 1978, ApJ, 221, L29
Blondin J. M., 1994, ApJ, 435, 756
Boccardi B. et al., 2021, A&A, 647, A67
Bright J. S. et al., 2020, Nat. Astron., 4, 697
Buchner J., 2014, Statistics and Computing, 26, 383
Buchner J., 2019, PASP, 131, 108005
Buchner J., 2021, J. Open Source Softw., 6, 3001
Campana S., Stella L., Mereghetti S., de Martino D., 2018, A&A, 610, A46
Chernyakova M., Malyshev D., Blay P., van Soelen B., Tsygankov S., 2020, MNRAS, 495, 365
Corbel S. et al., 2013b, MNRAS, 431, L107
Corbel S., Coriat M., Brocksopp C., Tzioumis A. K., Fender R. P., Tomsick J. A., Buxton M. M., Bailyn C. D., 2013a, MNRAS, 428, 2500
Corbel S., Fender R. P., Tomsick J. A., Tzioumis A. K., Tingay S., 2004, ApJ, 617, 1272
Coriat M. et al., 2011, in Romero G. E., Sunyaev R. A., Belloni T., eds, Proc. IAU Symp. 275, Jets at All Scales. Kluwer, Dordrecht, p. 255
De Becker M., Raucq F., 2013, A&A, 558, A28
de Jager O. C., Harding A. K., Michelson P. F., Nel H. I., Nolan P. L., Sreekumar P., Thompson D. J., 1996, ApJ, 457, 253
de la Cita V. M., Bosch-Ramon V., Paredes-Fortuny X., Khangulyan D., Perucho M., 2017, A&A, 598, A13
del Palacio S., Bosch-Ramon V., Romero G. E., Benaglia P., 2016, A&A, 591, A139
Dinçer T., Bailyn C. D., Miller-Jones J. C. A., Buxton M., MacDonald R. K. D., 2018, ApJ, 852, 4
Dougherty S. M., Pittard J. M., Kasian L., Coker R. F., Williams P. M., Lloyd H. M., 2003, A&A, 409, 217
Drury L. O., 1983, Rep. Prog. Phys., 46, 973
Eichler D., Usov V., 1993, ApJ, 402, 271
Falcke H., Körding E., Markoff S., 2004, A&A, 414, 895
Fransson C., Fabian A. C., 1980, A&A, 87, 102
Friend D. B., Abbott D. C., 1986, ApJ, 311, 701
Gallo E. et al., 2014, MNRAS, 445, 290
Gallo E., Fender R. P., Miller-Jones J. C. A., Merloni A., Jonker P. G., Heinz S., Maccarone T. J., van der Klis M., 2006, MNRAS, 370, 1351
Gallo E., Fender R. P., Pooley G. G., 2003, MNRAS, 344, 60
Gallo E., Miller B. P., Fender R., 2012, MNRAS, 423, 590
Ghosh P., Lamb F. K., Pethick C. J., 1977, ApJ, 217, 578
H. E. S. S. Collaboration, 2020, A&A, 635, A167
Haberl F., White N. E., Kallman T. R., 1989, ApJ, 343, 409
Hales C. A., Benaglia P., del Palacio S., Romero G. E., Koribalski B. S., 2017, A&A, 598, A42
Hamaguchi K. et al., 2018, Nat. Astron., 2, 731
Hannikainen D. C., Hunstead R. W., Campbell-Wilson D., Sood R. K., 1998, A&A, 337, 460
Heinz S., Sunyaev R. A., 2003, MNRAS, 343, L59
Higginbottom N., Knigge C., Sim S. A., Long K. S., Matthews J. H., Hewitt H. A., Parkinson E. J., Mangham S. W., 2020, MNRAS, 492, 5271
Johnstone C. P., Zhilkin A., Pilat-Lohinger E., Bisikalo D., Güdel M., Eggl S., 2015, A&A, 577, A122
Kaaret P., Feng H., Roberts T. P., 2017, ARA&A, 55, 303
King A., Lasota J.-P., 2016, MNRAS, 458, L10
Koliopanos F., Vasilopoulos G., 2018, A&A, 614, A23
Koljonen K. I. I., Maccarone T., McCollough M. L., Gurwell M., Trushkin S. A., Pooley G. G., Piano G., Tavani M., 2018, A&A, 612, A27
Kosec P. et al., 2021, MNRAS, 508, 3569
Kosec P., Pinto C., Walton D. J., Fabian A. C., Bachetti M., Brightman M., Fürst F., Grefenstette B. W., 2018, MNRAS, 479, 3978
Krtička J., 2014, A&A, 564, A70
Krtička J., Kubát J., Krtičková I., 2015, A&A, 579, A111
Krtička J., Kubát J., Krtičková I., 2018, A&A, 620, A150
Krtička J., Owocki S. P., Meynet G., 2011, A&A, 527, A84
Kudritzki R.-P., Puls J., 2000, ARA&A, 38, 613
Kylafis N. D., Contopoulos I., Kazanas D., Christodoulou D. M., 2012, A&A, 538, A5
Lamers H. J. G. L. M., Cassinelli J. P., 1999, Introduction to Stellar Winds. Cambridge Univ. Press, Cambridge
Lemaster M. N., Stone J. M., Gardiner T. A., 2007, ApJ, 662, 582
Li K. L., Hu C. P., Lin L. C. C., Kong A. K. H., 2016, ApJ, 828, 74
Maccarone T. J., 2005, MNRAS, 360, L68
Maravelias G., Kraus M., Cidale L. S., Borges Fernandes M., Arias M. L., Curé M., Vasilopoulos G., 2018, MNRAS, 480, 320
Markoff S., Falcke H., Fender R., 2001, A&A, 372, L25
Markoff S., Nowak M., Corbel S., Fender R., Falcke H., 2003, A&A, 397, 645
Martin R. G., Nixon C., Armitage P. J., Lubow S. H., Price D. J., 2014, ApJ, 790, L34
Massi M., Kaufman Bernadó M., 2008, A&A, 477, 1
McClintock J. E., Remillard R. A., 2006, Black Hole Binaries. Cambridge University Press, UK, p. 157
Meier D. L., Koide S., Uchida Y., 2001, Science, 291, 84
Merloni A., Heinz S., di Matteo T., 2003, MNRAS, 345, 1057
Middleton M., Higginbottom N., Knigge C., Khan N., Wiktorowicz G., 2021, MNRAS, 509, 1119
Migliari S., Fender R. P., 2006, MNRAS, 366, 79
Mushtukov A. A., Ingram A., Middleton M., Nagirner D. I., van der Klis M., 2019, MNRAS, 484, 687
Okazaki A. T., Hayasaki K., Moritani Y., 2013, PASJ, 65, 41
Oosterbroek T. et al., 1997, A&A, 321, 776
Parfrey K., Spitkovsky A., Beloborodov A. M., 2016, ApJ, 822, 33
Parfrey K., Tchekhovskoy A., 2017, ApJ, 851, L34
Parkin E. R., Pittard J. M., 2008, MNRAS, 388, 1047
Petropoulou M., Kamble A., Sironi L., 2016, MNRAS, 460, 44
Petropoulou M., Vasilopoulos G., Christie I. M., Giannios D., Coe M. J., 2018, MNRAS, 474, L22
Pittard J. M., Dougherty S. M., Coker R. F., O'Connor E., Bolingbroke N. J., 2006, A&A, 446, 1001
Pittard J. M., Romero G. E., Vila G. S., 2021, MNRAS, 504, 4204
Pittard J. M., Vila G. S., Romero G. E., 2020, MNRAS, 495, 2205
Porter J. M., Rivinius T., 2003, PASP, 115, 1153
Poutanen J., Lipunova G., Fabrika S., Butkevich A. G., Abolmasov P., 2007, MNRAS, 377, 1187
Razin V. A., 1960, Izuestiya Vys. Ucheb. Zaued. Radiofiz., 3, 921
Reig P., 2011, Ap&SS, 332, 1
Reig P., Fabregat J., Alfonso-Garzón J., 2020, A&A, 640, A35
Reimer A., Pohl M., Reimer O., 2006, ApJ, 644, 1118
Rodríguez L. F., Arthur J., Montes G., Carrasco-González C., Toalá J. A., 2020, ApJ, 900, L3
Russell D. M. et al., 2013, MNRAS, 429, 815
Sari R., Piran T., Narayan R., 1998, ApJ, 497, L17
Selina R. J. et al., 2018, in Marshall H. K., Spyromilio J., eds, Proc. SPIE Conf. Ser. Vol. 10700, Ground-Based and Airborne Telescopes VII. SPIE, Bellingham, p. 107001O
Shakura N. I., Sunyaev R. A., 1973, A&A, 24, 337
Takahashi H. R., Ohsuga K., 2017, ApJ, 845, L9
Tchekhovskoy A., Narayan R., McKinney J. C., 2011, MNRAS, 418, L79
Tetarenko B. E., Lasota J. P., Heinke C. O., Dubus G., Sivakoff G. R., 2018, Nature, 554, 69
Tsygankov S. S., Doroshenko V., Mushtukov A. A., Lutovinov A. A., Poutanen J., 2018, MNRAS, 479, L134
Usov V. V., 1992, ApJ, 389, 635
van den Eijnden J. et al., 2019b, MNRAS, 487, 4355
van den Eijnden J. et al., 2020, Astron. Telegram, 14193, 1
van den Eijnden J. et al., 2021, MNRAS, 507, 3899
van den Eijnden J., Degenaar N., Russell T. D., Hernández Santisteban J. V., Wijnands R., Miller-Jones J. C. A., Rouco Escorial A., Sivakoff G. R., 2019a, MNRAS, 483, 4628

van den Eijnden J., Degenaar N., Russell T. D., Miller-Jones J. C. A., Wijnands R., Miller J. M., King A. L., Rupen M. P., 2018a, MNRAS, 473, L141
van den Eijnden J., Degenaar N., Russell T. D., Miller-Jones J. C. A., Wijnands R., Miller J. M., King A. L., Rupen M. P., 2018b, MNRAS, 474, L91
van den Eijnden J., Degenaar N., Russell T. D., Wijnands R., Miller-Jones J. C. A., Sivakoff G. R., Hernández Santisteban J. V., 2018c, Nature, 562, 233
van der Horst A. J. et al., 2013, MNRAS, 436, 2625
van der Merwe C. J. T., Wadiasingh Z., Venter C., Harding A. K., Baring M. G., 2020, ApJ, 904, 91
Vasilopoulos G., Koliopanos F., Haberl F., Treiber H., Brightman M., Earnshaw H. P., Gúrpide A., 2021, ApJ, 909, 50
Vasilopoulos G., Lander S. K., Koliopanos F., Bailyn C. D., 2020, MNRAS, 491, 4949
Vasilopoulos G., Petropoulou M., Koliopanos F., Ray P. S., Bailyn C. B., Haberl F., Gendreau K., 2019, MNRAS, 488, 5225
Vink J. S., de Koter A., Lamers H. J. G. L. M., 2000, A&A, 362, 295
Vlahakis N., 2015, Theory of Relativistic Jets. Springer International Publishing, Switzerland, p. 177
Vlahakis N., Königl A., 2004, ApJ, 605, 656
Watson S. K., Davis R. J., Williams P. M., Bode M. F., 2002, MNRAS, 334, 631
Werner M., Reimer O., Reimer A., Egberts K., 2013, A&A, 555, A102
Wilson-Hodge C. A. et al., 2018, ApJ, 863, 9
Wolff M. T. et al., 2016, ApJ, 831, 194
Wright A. E., Barlow M. J., 1975, MNRAS, 170, 41
Yuan F., Cui W., Narayan R., 2005, ApJ, 620, 905
Zdziarski A. A., 2012, MNRAS, 422, 1750

APPENDIX A: OPTICAL DEPTH FOR FREE–FREE ABSORPTION BY THE STELLAR WIND

For a general path (not going through the star), the optical depth for free–free absorption by the stellar wind can be calculated as (Wright & Barlow 1975)

$$\tau_\nu^{\rm ff} = K(\nu, T) \int_0^{+\infty} {\rm d}l \, \frac{A^2}{r^4}, \tag{A1}$$

where A and $K(\nu, T)$ are defined in equations (9) and (10), respectively. Ignoring the curvature of the shock, we compute the optical depth for paths above and below the apex as shown in Fig. A1, as well as through the apex itself.

For a path with $z_{\rm o} = 0$, equation (A1) becomes

$$\tau_\nu^{\rm ff} = K(\nu, T) \frac{A^2}{q^3} \int_{-i}^{+\pi/2} {\rm d}\theta \cos^2\theta, \tag{A2}$$

after changing the variable of integration from l to θ, using that $l = R_{\rm Be}\sin i + q\tan\theta$, ${\rm d}l = (q/\cos^2\theta){\rm d}\theta$, and $q = R_{\rm Be}\cos i = r\cos\theta$.

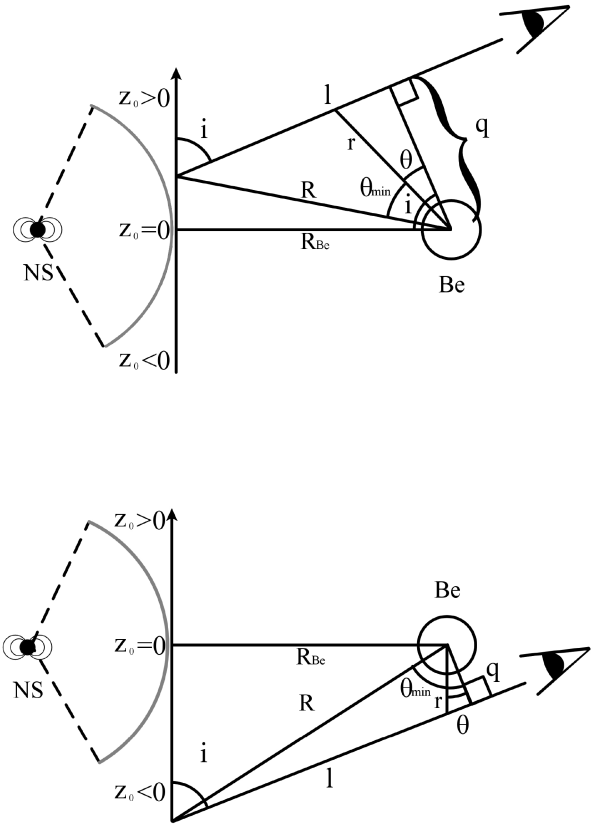

Figure A1. Sketch of the geometry assumed for the free–free optical depth calculation. For an explanation of symbols, see the text.

The above equation can be generalized for paths with $z_o \neq 0$ as

$$\tau_\nu^{\rm ff} = K(\nu, T)\frac{A^2}{q^3}\int_{-\theta{\rm min}}^{+\pi/2} {\rm d}\theta \cos^2\theta, \tag{A3}$$

where we used $l = \sqrt{z_o^2 + R_{\rm Be}^2}\sin\theta_{\rm min} + q\tan\theta$. Here,

$$\theta_{\rm min} = i - \tan^{-1}\left(\frac{|z_o|}{R_{\rm Be}}\right) \text{ and} \tag{A4}$$

$$q = \sqrt{z_o^2 + R_{\rm Be}^2}\cos\theta_{\rm min}. \tag{A5}$$

APPENDIX B: ANALYTICAL DERIVATION OF THE $L_{\rm R}$–$L_{\rm X}$ RELATION

In this section, we derive the scaling relation between the radio and X-ray luminosities expected in our model whenever the radio band is dominated by optically thin synchrotron emission produced in the wind collision region. We also focus on the slow-cooling regime for radio-emitting electrons.

Let $L_{\rm R}$ be the optically thin synchrotron luminosity at frequency $\nu_{\rm R}$, i.e.

$$L_{\rm R} \equiv P_{\rm syn}(\nu_{\rm R}) = \frac{4}{3}\sigma_{\rm T} c U_{\rm B}\gamma_{\rm R}^2\nu_{\rm R}^{-1}\left(n_{\gamma_{\rm R}}\gamma_{\rm R}\right)V_{\rm em}, \tag{B1}$$

where $V_{\rm em} = 4\pi f_{\rm V} R_{\rm sh}^3$ is the emitting volume of the wind collision region with $f_{\rm V} \approx 1/4$, $\gamma_{\rm R} = \{2\pi m_{\rm e} c\nu_{\rm R}/[e(8\pi U_{\rm B})^{1/2}]\}^{1/2}$ is the Lorentz factor of synchrotron-emitting electrons at $\nu_{\rm R}$, and $\left(n_{\gamma_{\rm R}}\gamma_{\rm R}\right)$ is the number density of electrons radiating at $\nu_{\rm R}$. For the derivation of the equation, we assume that each electron emits at the characteristic synchrotron frequency.

Henceforth, we focus on cases with $\nu_{\rm R} < \nu_{\rm c}$, where $\nu_{\rm c}$ is the characteristic synchrotron cooling frequency. Using also equations (1)–(5) and noting that $R_{\rm sh} = \min(d_{\rm NS}, d_{\rm Be})$, the radio luminosity at $\nu_{\rm R}$ (see equation B1) is written as

$$L_{\rm R} \simeq C_1(p) f(p) L_{\rm X}^{\frac{12}{7}} \nu_{\rm R}^{\frac{-p+1}{2}} \left(\dot{M}_{\rm Be} V_{\rm Be}^{\infty}\right)^{\frac{p-1}{4}} \epsilon_{\rm B}^{\frac{p+1}{4}} \epsilon_{\rm e} \epsilon^{-\frac{12}{7}} (\eta_{\rm out}\chi)^{\frac{3}{2}} \xi^{-\frac{3}{4}} \mu_{\rm NS}^{-\frac{3}{7}} D^{\frac{1-p}{2}} \tag{B2}$$

for $\eta \gg 1$. Here,

$$f(p) = \begin{cases} (p-2)\gamma_{\rm min}^{p-2}, & p > 2 \text{ and } \gamma_{\rm max} \gg \gamma_{\rm min} \\ \ln^{-1}\left(\frac{\gamma_{\rm max}}{\gamma_{\rm min}}\right), & p = 2 \end{cases} \tag{B3}$$

and

$$C_1(p) = \frac{2^{\frac{3}{28}}\sigma_{\rm T} e^{\frac{-3+p}{2}}}{24\, c^{\frac{24}{7}}}\left(\frac{9}{4}\right)^{\frac{5+p}{4}} (2\pi m_{\rm e} c)^{\frac{-p+1}{2}} (G M_{\rm NS})^{\frac{6}{7}} f_{\rm V}. \tag{B4}$$

Hence, for $\eta \gg 1$ (or $L_{\rm X} \ll L_{\rm X,br}$; see equation 14) and $p = 2$ the predicted relation is

$$L_{\rm R} \simeq 10^{18} L_{\rm X,38}^{\frac{12}{7}} \nu_{\rm R,10}^{-\frac{1}{2}} \left(\dot{M}_{\rm Be,-9} V_{\rm Be,3}^{\infty}\right)^{\frac{1}{4}} \epsilon_{\rm B,-0.3}^{\frac{3}{4}} \epsilon_{\rm e,-0.3} \epsilon_{-1}^{-\frac{12}{7}} (\eta_{\rm out,-2}\,\chi_0)^{\frac{3}{2}} \xi_{-0.3}^{-\frac{3}{4}} \mu_{\rm NS,30}^{-\frac{3}{7}} D_{13}^{-\frac{1}{2}} \ln^{-1}\left(\frac{\gamma_{\rm max}}{\gamma_{\rm min}}\right) {\rm erg\,s^{-1}\,Hz^{-1}}, \tag{B5}$$

where we introduced the notation $q_x \equiv q/10^x$ in cgs units, except for the Be mass-loss rate that is in units of $\rm M_\odot\,yr^{-1}$ and the wind velocity that is in units of $\rm km\,s^{-1}$.

Similarly, we derive the expression for $\eta \ll 1$, which reads

$$L_{\rm R} \simeq C_2(p) f(p) L_{\rm X}^{\frac{2(p-1)}{7}} \nu_{\rm R}^{\frac{-p+1}{2}} \left(\dot{M}_{\rm Be} V_{\rm Be}^{\infty}\right)^{\frac{3}{2}} \epsilon_{\rm B}^{\frac{p+1}{4}} \epsilon_{\rm e}\, \epsilon^{\frac{2(1-p)}{7}} (\eta_{\rm out}\chi)^{\frac{p-1}{4}} \xi^{\frac{1-p}{8}} \mu_{\rm NS}^{\frac{1-p}{14}} D^{\frac{1-p}{2}} \tag{B6}$$

with C_2 given by

$$C_2(p) = \frac{2^{\frac{p-1}{56}}\sigma_{\rm T} e^{\frac{-3+p}{2}}}{24\, c^{\frac{4(p-1)}{7}}}\left(\frac{9}{4}\right)^{\frac{5+p}{4}} (2\pi m_{\rm e} c)^{\frac{-p+1}{2}} (G M_{\rm NS})^{\frac{p-1}{7}} f_{\rm V}. \tag{B7}$$

Hence, for $\eta \ll 1$ (or $L_{\rm X} \gg L_{\rm X,br}$) and $p = 2$, the expected radio-X-ray luminosity relation reads

$$L_{\rm R} \simeq 3.5\times 10^{17} L_{\rm X,38}^{\frac{2}{7}} \nu_{\rm R,10}^{-\frac{1}{2}} \left(\dot{M}_{\rm Be,-9} V_{\rm Be,3}^{\infty}\right)^{\frac{3}{2}} \epsilon_{\rm B,-0.3}^{\frac{3}{4}} \epsilon_{\rm e,-0.3} \epsilon_{-1}^{-\frac{2}{7}} (\eta_{\rm out,-2}\,\chi_0)^{\frac{1}{4}} \xi_{-0.3}^{-\frac{1}{8}} \mu_{\rm NS,30}^{-\frac{1}{14}} D_{13}^{-\frac{1}{2}} \ln^{-1}\left(\frac{\gamma_{\rm max}}{\gamma_{\rm min}}\right) {\rm erg\,s^{-1}\,Hz^{-1}}. \tag{B8}$$

APPENDIX C: CORNER PLOTS

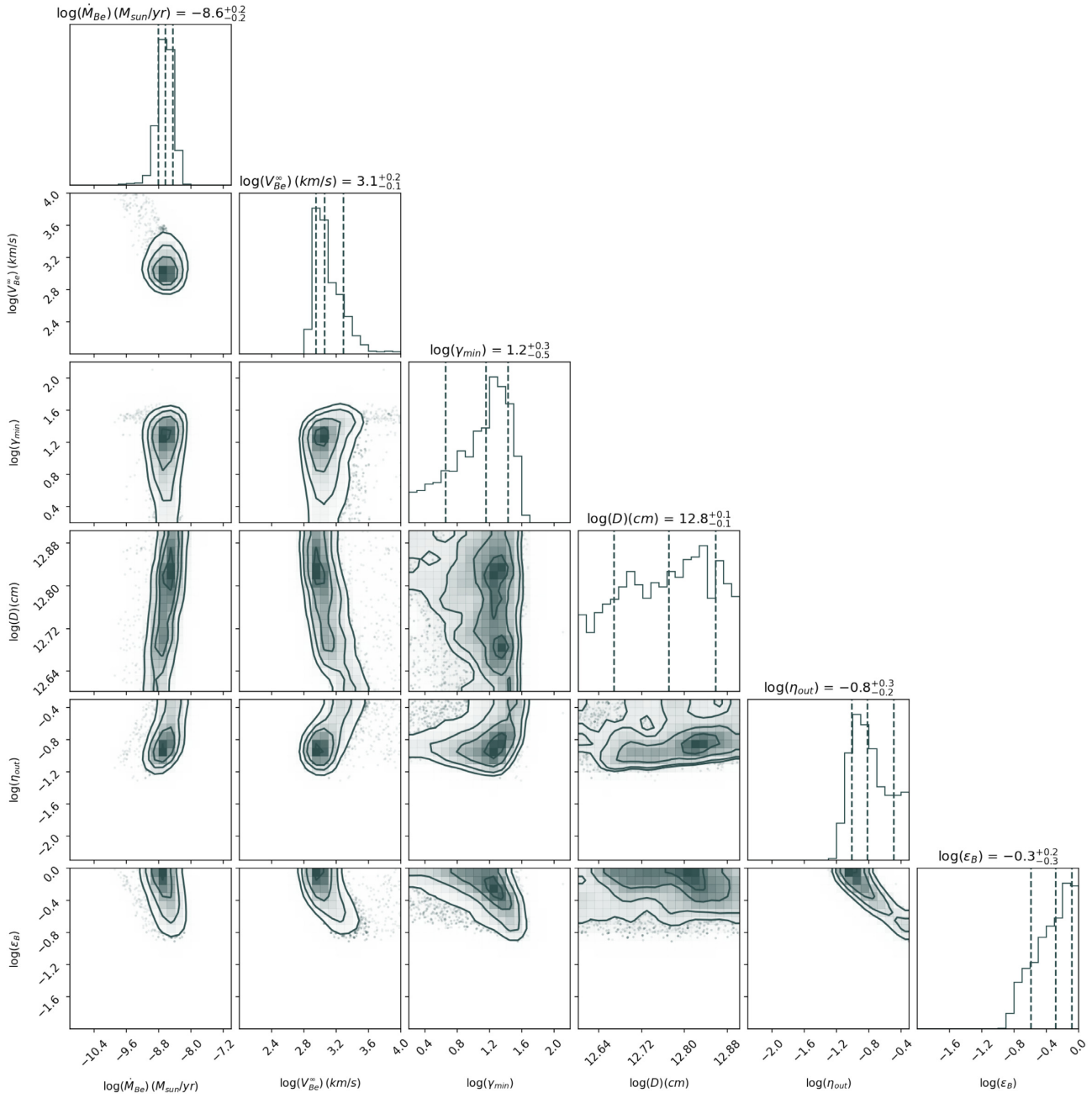

Figure C1. Corner plot of the parameter pairs and the marginal posterior distributions for epoch A. Dashed vertical lines indicate the median and the 68 per cent range for each parameter.

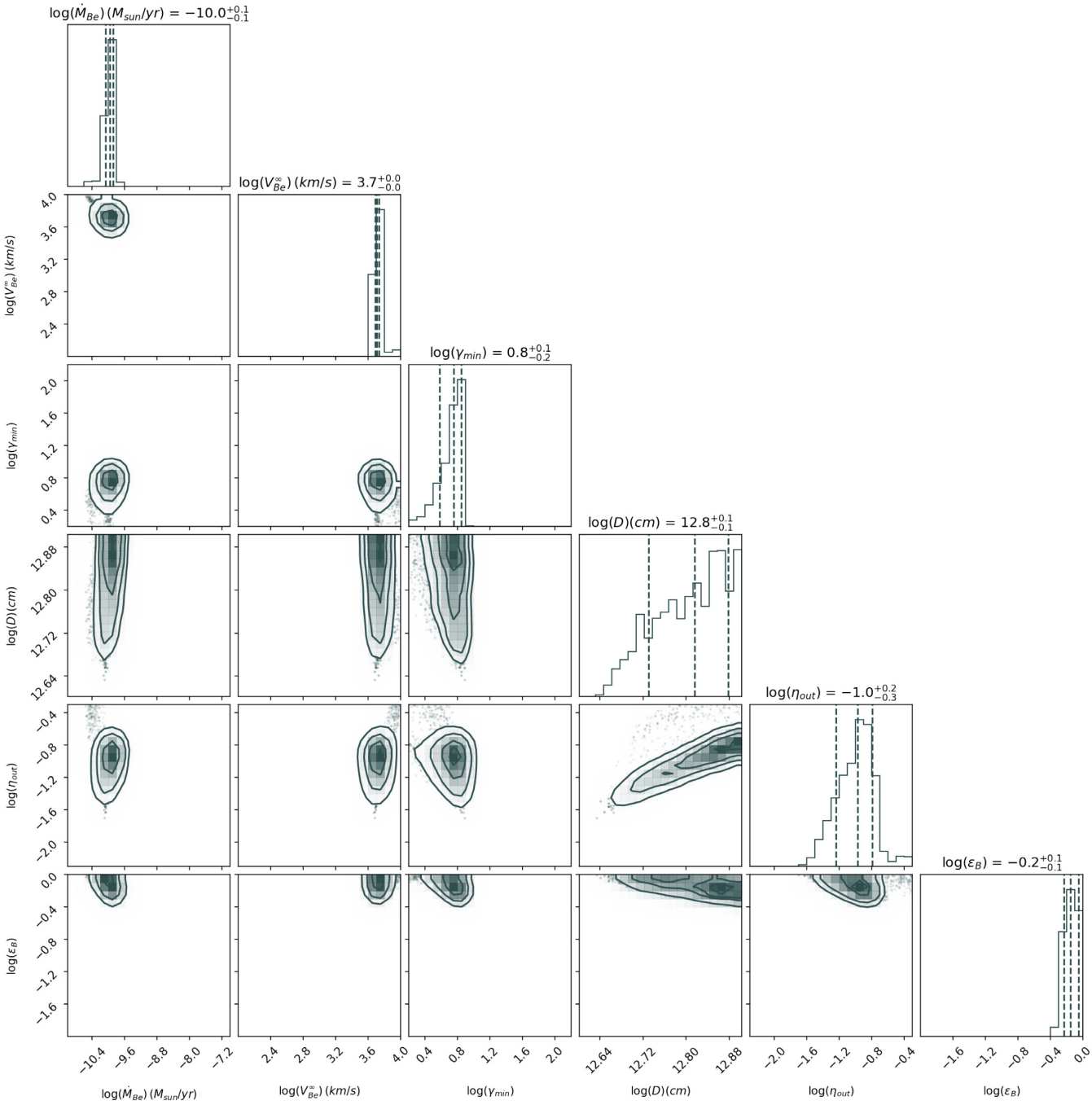

Figure C2. Corner plot of the parameter pairs and the marginal posterior distributions for epoch B. Dashed vertical lines indicate the median and the 68 per cent range for each parameter.

This paper has been typeset from a TEX/LATEX file prepared by the author.